PROCESSING–STRUCTURE–PROPERTY RELATIONSHIPS OF SPARK PLASMA SINTERED BORON CARBIDE AND TITANIUM DIBORIDE CERAMIC COMPOSITES

William S. Rubink, B.S.

Thesis Prepared for the Degree of

MASTER OF SCIENCE

UNIVERSITY OF NORTH TEXAS

May 2018

APPROVED:

Thomas W. Scharf, Major Professor
Jincheng Du, Committee Member
Richard F. Reidy, Committee Member
Andrey Voevodin, Chair of the Department of Materials Science and Engineering
Costas Tsatsoulis, Dean of the College of Engineering
Victor Prybutok, Dean of the Toulouse Graduate School

Rubink, William S. *Processing–Structure–Property Relationships of Spark Plasma Sintered Boron Carbide and Titanium Diboride Ceramic Composites*. Master of Science (Materials Science and Engineering), May 2018, 50 pp., 5 tables, 22 figures, references, 26 titles.

The aim of this study was to understand the processing – structure – property relationships in spark plasma sintered (SPS) boron carbide (B4C) and B4C-titanium diboride (TiB2) ceramic composites. SPS allowed for consolidation of both B4C and B4C-TiB2 composites without sintering additives, residual phases, e.g., graphite, and excessive grain growth due to long sintering times. A selection of composite compositions in 20% TiB2 feedstock powder increments from 0% to 100%, was sintered at 1900°C for 25 minutes hold time. A homogeneous B4C-TiB2 composite microstructure was determined with excellent distribution of TiB2 phase, while achieving ~99.5% theoretical density. An optimum B4C-23 vol.% TiB2 composite composition with low density of ~3.0 g/cm3 was determined that exhibited ~30-35% increase in hardness, fracture toughness, and flexural bend strength compared to commercial armor-grade B4C. This is a result of a) no residual graphitic carbon in the composites, b) interfacial microcrack toughening due to thermal expansion coefficient differences placing the B4C matrix in compression and TiB2 phase in tension, and c) TiB2 phase aids in crack deflection thereby increasing the amount of intergranular fracture. Collectively, the addition of TiB2 serves as a strengthening and toughening agent, and SPS shows promise for the manufacture of hybrid ceramic composites.

Copyright 2018

By

William S. Rubink

ACKNOWLEDGEMENTS

Thanks to the Army Research Laboratory for the funding to pursue this project; Specifically Drs. Dan Casem and Jeff Lloyd (program manager) for Guidance over the duration of my work on this study. Thanks to Dr. Eric J. Faierson at the Quad Cities Manufacturing Lab for the scaled samples that we could not make here. Thanks to Dr. Thomas Scharf, mentor and advisor through my undergraduate and graduate experience, and Drs. Richard F Reidy and Jincheng Du for being my committee members here at the University of North Texas. Dr. Rajarshi Banerjee for use of his Lab and the SPS system in particular. Thanks to Victor Ageh for help with SEM and ImageJ analysis, and thanks to Nathan Ley for his help with the synchrotron data acquisition and interpretation.

TABLE OF CONTENTS

Page

LIST OF TABLES

Page

LIST OF FIGURES

Page

LIST OF EQUATIONS

Page

CHAPTER 1

INTRODUCTION AND MOTIVATION

1.1 Introduction

In the search for optimal materials, there is always the concession from each property where change in one elicits change in another. The direct relationship between thermal and electrical conductivity, or the inverse relationship between toughness and hardness are popular examples. One old solution to this problem, filling in some of the gaps in the great material continuum, is the use of composites. Composites have an ancient history, bridging the gap between mud and straw, between pozzolan ash and monolithic stone, borrowing one's properties and lending to the other. More recently ceramic matrix composites have been explored with similar rationale. The study of Boron Carbide (B4C) within this thesis regards its use as a matrix or continuous phase with Titanium Di-Boride (TiB2) dispersed phase. The effect of a TiB2 secondary phase in different loadings on the microstructure and mechanical and fracture properties is studied with comparisons made to pure B4C and TiB2. In a similar manner to how fibers of straw or crushed rocks, respectively, lend their tensile or compressive strengths to the matrix, the TiB2 addition lends its fracture toughness and plasticity to the otherwise brittle B4C.

As a monolithic material B4C has a high hardness, low density, and unspectacular grey to black appearance. Its typical use is in ceramic armor plating against ballistic projectiles or as an abrasive medium. Aside from its use monolithically as armor, due to its hardness and or electrical properties, it is valued as an abrasive and in systems where its semi-conductivity is advantageous. Meanwhile TiB2 is grey in color, harder, denser, but most importantly, tougher than B4C. Like the aggregate in concrete, the TiB2 lends this

particular fracture toughness to the resultant material properties. Thus, when a crack is initiated, it is expected that the cracks will be stopped or deflected by the grains of TiB2 within the material.

How well this works depends on a collection of factors intrinsic to the starting materials and their particular properties. Some level of optimization occurs here, where material selection, processing, and relative fraction control the properties of the final product. Even though improvements have already been clearly made in related areas, a simple comparison of this composite over the current system and relevant alternatives is the real problem and purpose of this work. As an example, currently hot pressed B4C exhibits residual graphitic inclusions as a product of processing that are known to be detrimental to the ultimate strength and hardness of the material by providing points of stress concentration/crack initiation and softening, respectively. Thus, two important aims of this work are to eliminate the presence of the graphitic inclusions, and to introduce a homogeneously dispersed distribution of TiB2 to mitigate crack propagation.

Through this thesis, an examination of the currently used ceramic armor materials, bulk properties, and known processing characteristics will be made against B4C and TiB2 composites processed by spark plasma sintering. Comparisons will be made regarding processing methodologies, material and powder compositions, microstructure, residual stress states, mechanical and fracture properties, and then determine the strengthening and toughening mechanisms.

1.2 Motivation

With regard to the manufacture of ceramic components, there are a number of

factors that heavily influence material properties. These occur at many length scales and for a variety of reasons. It is the interest of this study then, to look primarily at how processing and composition affect the properties of finely grained single component ceramics versus the same in a homogeneously mixed ceramic composite. Not only is the investigation focused on the samples studied here, but how they compare to currently used state-of-the-art ceramic armor material systems.

CHAPTER 2

LITERATURE REVIEW

2.1 Overview of Sintering

Consolidation of ceramic samples is commonly achieved via sintering due to the high temperatures required to melt or sublime most industrial ceramics. The sintering process is one in which consolidation occurs at temperature significantly below that of the melting point of the material. The reason processing takes place at these lower temperatures is usually due to the prohibitively high temperatures required for a full melt even if molten materials may be formed much more easily. The particular dynamics of the sintering process depend on several factors, some of which are desired and others are best avoided.

Sintering typically follows a series of several phases that can be described empirically as well as thermodynamically. The first phase of sintering occurs when temperature allows for significant surface diffusion of the material. This surface diffusion brings particles with the highest surface energy, by lack of fully coordinated bonding from the faces, edges, and vertices, to points of lower energy. The lowest energies are those that best equate the fully coordinated intergranular regions to those where two grains are in contact. The high energy molecules then diffuse to these conjoining points beginning the process that is called necking. The second phase is the continued evolution of the necking to form grain boundaries since the particles are in unique orientations that preclude single crystal formation then eventually to the point that the free energy of the internal surface for that given environment has come to relative equilibrium. Often in this process pores are retained where a junction of several grains exists. The elimination of these pores can

be troublesome; however, their presence can be reduced by different sintering methodologies.

2.1.1 Pressureless Sintering

The most well-known sintering method is that of pressureless sintering. Although the technique can be quite controlled in laboratory settings, its earliest forms to create clay pottery were much less so. The basic procedure involves heating an agglomeration of unsintered particles held together by some sort of adhesive matrix or merely intermolecular forces. This "green" body is then heated at atmospheric pressures to some fraction of its melting point, typically at least 60 percent. The process of surface diffusion that drives the sintering in this case can be quite slow, so the green body is held around that temperature for some time before being allowed to cool. When complete, the sintered piece is typically smaller than its green form. This is a simple product of the closure of the pores, thus the higher the green density, the higher the final density. Modern techniques may vary the sintering atmosphere to be oxidizing, reducing, totally inert, or even reactive with atmospheres other than oxygen, carbon dioxide, or nitrogen. Since sintering occurs at near atmospheric pressures, it is referred to as pressureless sintering.

2.1.2 Hot Pressing and Hot Isostatic Pressing

It is often the case that pressureless sintering may not allow the formation of totally dense compacts, primarily through closure of the intergranular pores, in which case some form of pressure must be exerted. Many implementations of this exist, however, the two most commonly used in industry for parts are hot pressing, of which SPS is related, and hot

isostatic pressing (HIP). The basic premise behind each of these is exposure of a green part to high pressure from one or more directions. This can be done uni-axially, or isostatically in a gas, commonly argon, or by encapsulation and submersion in a liquid, usually an oil, to which the intense pressures are applied. The green parts are then exposed to high temperatures. In hot pressing, pressure is usually applied uni-axially, and heating of the sample is done by conduction, induction, or in-situ resistive heating. For HIP, resistive heating elements are internal to the pressure vessel and heat the parts via radiation and convection while the pressure vessel itself is water cooled. Implicitly this technique comes with a handful of advantages and disadvantages. The primary advantages are that parts can be compressed isostatically such that pressures exerted are applied against the whole of the part. Near net shape parts may be manufactured and machined to final tolerances. The other advantage and reason for use in industry is that the pressure chambers used to make the parts can be large and sizable parts of varying geometries may be produced in large numbers. The primary disadvantage to this technique lies in the rather extended periods of time that the part must be sintered. The time required to heat and cool the sample are often extended operations such that there are concerns with grain growth and energy costs. The high temperatures and pressures are also quite dangerous individually, and the combination of the two is exponentially so.

2.1.3 Spark Plasma Sintering

The processing method used in the work here however, sharing some similarities with the aforementioned, especially hot-pressing, is commonly called spark plasma sintering (SPS). It is worth noting that there is actually no appreciable spark plasma

generated by the system under typical conditions (Hulbert, 2008); however, the nomenclature remains in common use. SPS is a process by which a pulsed DC current is passed through a uniaxial press containing sample material in a die. The current induces resistive heating in the die and or material providing the heat requirements of sintering. It is this in-situ heating of the raw material, in addition to the uniaxial application of pressure that gives SPS the distinct advantage of both rapid and complete sintering. Where HIP might require the better part of 24 hours to complete a sample, the same can be done in SPS in less than one hour. The tradeoff of course is that while HIP may produce many parts of complex geometry, SPS will typically only produce one part of simple geometry. Due to the short times in SPS, it is possible to avoid significant grain growth that can degrade mechanical and fracture properties. Just as with the other methods of sintering, the quality of the starting material can have a large impact on the results.

2.2 Sintering of B_4C, TiB_2, and Their Composites

For this study, although the specific composite matrix material was pre-decided due to it being a low density armor material, there was some flexibility of the dispersed secondary phase. TiB2 for reasons mentioned above was chosen; however, an equiatomic TiB phase was initially targeted since it often exhibits acicular or needle-like shapes that was conjectured to provide a more tortuous path for cracks to propagate and thus toughen the composite. The formation of TiB2 is preferred over that of TiB at the temperatures and pressures defined by the study's processing parameters. This is clear by the Gibbs free energy of formation for 1 mol of each, $-5.03*10^5$J for TiB2 and $-3.48*10^5$J for TiB (Bale, 2016). It is also worth noting that the typical methods of production of both B4C and TiB2

can result in surface impurities in the form of B2O3 as a surface oxide on both powders, and TiO2, on the TiB2. Fact-Web calculations (Table 1) show the formation of both oxides on their respective powders (Bale, 2016). There is also the presence of carbon in the punch and die and shielding foils. This carbon is non-reactive. This leads to a conundrum concerning input and output ratios of B4C to TiB2 which will be discussed later. As in all material selection queries, the matter of cost was a big decider for the starting material size. Initially a relatively coarse material (325 Mesh) was chosen and subsequently milled in a high energy ball mill. However, a finer powder size was chosen to circumvent the milling step, and also lead to improved material properties. Also, the use of nanometer size B4C starting powder was not pursued due to the high cost and additional difficulties with some test samples of the sintered material. Despite the problems with the nanometer powders, interesting elements of processing showed up in preliminary tests indicating potential for future studies.

Table 1 - Equilibrium State Surface Oxides at 273K, 1Atm

Input				Output		
grams	Compound	state		grams	Compound	state
1.00	Ar	Gas	>	1.00	Ar	Gas
1.00	C	Solid	>	1.00	C	Solid
1.00	B_4C	Solid	>	1.00	B_4C	Solid
1.60E-11	O_2	Gas	>	2.32E-11	B_2O_3	Solid
			>	1.97E-49	CO	Gas
			>	4.22E-67	$(BO)_2$	Gas
Input				Output		
grams	Compound	state		grams	Compound	state
1.00	Ar	Gas	>	1.00	Ar	Gas
1.00	C	Solid	>	1.00	C	Solid
1.00	TiB_2	Solid	>	1.00	TiB_2	Solid
1.60E-11	O_2	Gas	>	1.55E-11	B_2O_3	Solid
			>	1.60E-11	Ti_2O_3	Solid

The B4C system conveniently affords a few features for sintering. Although the temperatures for sintering B4C are quite high, sintering aids are not typically required due to some intrinsic properties of the powder used. Sintering aids are often used in the sintering process of other materials to aid in the physical compaction and reduction of porosity by providing a lower friction surface for particulates to rearrange, improving joining properties as an adhesive agent, diffusing more easily to fill gaps, or any combination thereof. Boron carbide, by nature of its composition possesses a native oxide layer. This boron glass has a low melting point relative to the B4C and gives the particles some ability to rearrange at temperatures below that at which the B4C begins to sinter. This is true to some degree for pressureless sintering, especially in the presence of oxygen, where the B4C may convert to B2O3 and CO. It is not the case, or at least minimally so, in the case of SPS which is done in a vacuum or inert atmosphere. By the time the B4C begins to sinter properly the boron glass has vaporized or reacted, leaving a homogeneous B4C bulk. High temperature plastic deformation in B4C also assists in achievement of high densities (Wei, 2015).

TiB_2 however, is a little more difficult to sinter, requiring higher temperatures and pressures compared to the B4C and composite parameters. This is mostly a product of a native TiO2 and B2O3 surface layer on the powder itself (Basu, 2006). Basu also notes that there is significant grain coarsening with TiB2 at high temperatures. Although this was evident in the study's samples, it did not prove to be a significant concern due to separation by the matrix. In test samples where TiB2 was more dominant however, it was more prominent.

2.3 Material Properties

2.3.1 Boron Carbide (B_4C)

Boron carbide is on the far end of the spectrum of materials in terms of specific strength. Given the motivation of this study's materials, density is an important factor. The armor plates will be worn or mounted on equipment and the ultimate mass must be considered. B4C has a remarkably low density of about 2.52g/cm^3. It has an elastic modulus of 446 GPA (Vargas-Gonzalez, 2010), which is quite high albeit not that critical a material property for armor materials. The more common and relevant property is that of Vickers or Knoop hardness which for the current armor HIP PAD B4C is 2632 kg/mm^2 and 2020 kg/mm^2, respectively (Vargas-Gonzalez, 2010). Also, there are several other material properties that are important to the armor applications. The fracture toughness, academically known as the stress intensity factor (K_{IC}), is a measure of force required to propagate a crack and is typically in the units of MPa*m$^{1/2}$. For PAD-B4C, this is a low value of about 2.9 MPa*m$^{1/2}$ (Vargas-Gonzalez, 2010). Also relevant is the ability to initiate a crack. This is not as easily quantified and is often tested empirically, as in this study, by fracture of bar samples. For B4C the flexural strength is about 398 MPa (Vargas-Gonzalez, 2010). The quantification of each of the material properties referenced here then provides a benchmark by which to understand this study's SPS pure B4C and B4C-TiB2 composites. The low density of the material allows for significant weight savings, the high hardness resists deflection and aids in the fracture of the impacting objects, the flexural strength reduces the probability or magnitude of fracture, and in the case of fracture the fracture toughness increases the energy that the material can absorb through fracture.

2.3.2 Titanium Diboride (TiB_2)

TiB2 on the other hand is significantly denser than B4C with a density of about 4.52g/cm^3. The addition of the TiB2 then will increase the density of the composite material. The elastic modulus of TiB2 is also quite high at 565 GPa, higher than B4C, however, its flexural strength is roughly the same at 400 MPa (Munro, 2000). The real benefit that TiB2 provides in the composite is it fracture toughness that is more than twice that of B4C at 6.9 MPa*m$^{1/2}$ (Munro, 2000). TiB2 typically finds use in a handful of situations some of which are in armor systems and wear resistant coatings. Figure 1 shows the eutectic B4C-TiB2 binary phase diagram (Rudy, 1966). It is evident that there is a large compositional range for the eutectic microstructure to be sintered with a clearly defined matrix and dispersed phase.

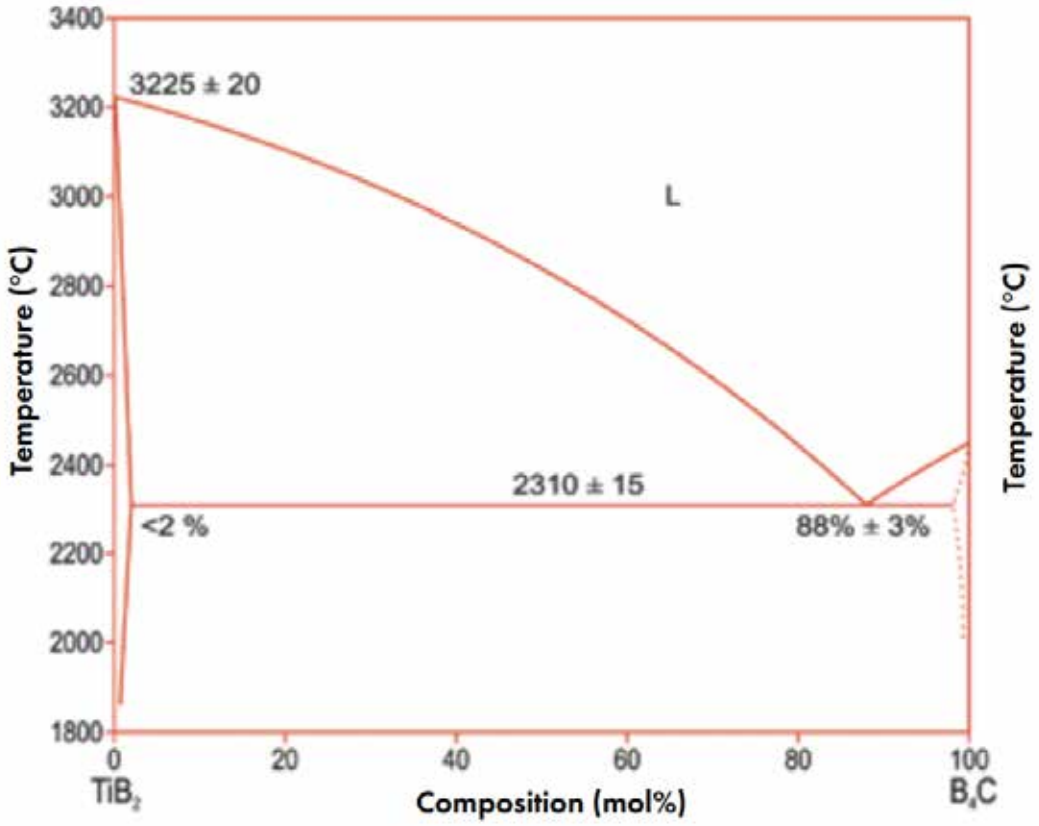

Figure 1 - Equilibrium Phase Diagram of TiB2-B4C (Rudy, 1966)

2.3.3 Silicon Carbide (SiC) and Silicon Carbon-Nitride (SiC-N)

The secondary point of comparison then was the compositional blend of B4C and TiB2 such that the composite density was equivalent to that of SiC at 3.2 g/cm^3. With this equivalent density, or potentially equivalency in other properties, properties could be compared for efficacy to armor materials. Although the only property of SiC that is significantly superior to B4C is its flexural strength at 487 MPa, a similar material SiC-N is much stronger at 578 MPa (Vargas-Gonzalez, 2010). Additionally the fracture toughness, though short of TiB2, is between 2.5 $MPa*m^{1/2}$ (SiC) and 4.5 $MPa*m^{1/2}$ (SiC-N) (Vargas-Gonzalez, 2010). Certainly the use of composites based on these materials could optimize some of these properties that will be determined and compared in this study.

CHAPTER 3

EXPERIMENTAL METHODS

3.1 Composite Processing

The bulk of this study used SPS as a method to fabricate the ceramic composites, x-ray diffraction to determine the resulting phases and crystal structures, and scanning electron microscopy (SEM) to determine grain size and volume fraction of phases. This was followed by Vickers micro-hardness testing to determine hardness and estimate fracture toughness, and three-point bend testing to quantify flexural (bend) strength.

3.1.1 Spark Plasma Sintering (SPS) System

A Thermal Technologies Inc. 10-3 Spark Plasma Sintering (SPS) system was utilized to process the ceramic composites, shown in Figure 2 and Figure 3. Spark plasma sintering is also known as pulsed electric current sintering. This system functions by two primary actions, uniaxial compression and the passing of Direct Current through the sample and its containing die. A series of 10kW Low Frequency Power modules provides the pulsed DC current, 3kA maximum, at a standard setting of 30ms on and 2ms off. Uniaxial pressure is applied by a Parker H-Pak hydraulic system which moves a steel piston rod up and down relative to the static steel anvil. The piston rod's movement is tracked by a Temposonics L-series position sensor and pressure is tracked by an Interface 25Klbf load cell below the hydraulic system. Temperature of the system is monitored by a thermocouple or infrared pyrometer depending on operating temperatures. Development of the parameters of operations was an iterative process which in most cases resulted in specimens of nearly full density/percent theoretical density, and exhibiting substantially improved properties,

presented later in Table 5 , compared to the commercially hot isostatic pressed samples that exhibit secondary phases such as graphite, and sintering additives (Vargas-Gonzalez, 2010).

Figure 2 – SPS Furnace and Control Cabinet

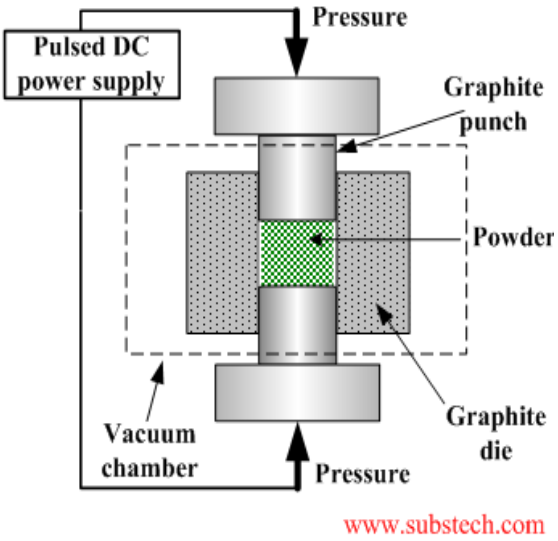

Figure 3 - SPS Sample Setup Diagram

3.1.2 Graphite Tooling

For the sintering of the samples, graphite tooling was used to contain the samples. Between the steel rams, several graphite parts are used to align and contain the samples. Sequentially by proximity to the rams, shown in Figure 3, are the cold-ram spacers which act primarily to distribute the load. Sintering spacers are next and these vary in geometry depending on the type of punch and die used. Next are the graphite punches and the die that contains the sample. Graphite foil, 0.13 mm thickness, is used to protect the graphite punch and die and aid in sample extraction. Large discs of foil are used to aid in distributing physical forces between the piston ram and cold-ram spacers. Smaller discs are used to separate the sample from the faces of the punch while a cylinder of foil separates the die from the sample and punches. The graphite tooling is purchased directly from Thermal Technologies. The shielding discs are cut by steel arch punches and the shielding cylinders are measured and cut with precision on a paper guillotine. High precision is required for the sheets, formed into cylinders, such that sintering material may not come in contact with the die. In the case of sample material adhering to either punch or die, scraping and cleaning can be done with machinist's blocks and plug gauges within a few microns of the target hole diameter. Also important to the operation of the die is graphite wool insulation which provides more consistent temperature regulation and reduced power consumption. Graphite twine is used to bind the graphite wool insulation.

3.1.3 Milling and Mixing

Mixing and homogenizing of the powders was done on a twin roller machine in high density polyethylene (HDPE) bottles. Rolling and mixing of the powders was with 10mm

diameter tungsten carbide balls. Tungsten carbide was chosen, due to hardness and toughness, to reduce the possibility of media contamination. Likewise, the HDPE bottles were used instead of traditional ceramic jars not only to reduce contamination but because milling was not required. Enough balls were introduced to line the length of the jar. The media added a mechanical force to shear agglomerates and ensure thorough mixing. Powders were rolled for 24 hours at approximately 400 rpm, or about 200 linear fpm. This resulted in well mixed and distributed powders. Due to the small size of the particles, a powder distribution was not made on the materials as received. After 24 hours of milling, powders were sieved through a coarse screen to separate the mixing media and returned to the jar. The media was then ultrasonically cleaned in dilute detergent for 15 minutes and rinsed with Isopropanol and set aside to air dry.

There were attempts early in the study to dry-mill the powders both together and separately in a high energy ball mill but no significant improvement in the grain size distribution was found. There could be potential in revisiting this option in future studies with a change to wet-milling.

3.1.4 Sample Setup and Furnace Operation

Production of samples initially involved significant research into prior SPS studies of B4C (Heydari, 2015) (Schaeffer, 2014). Table 2, partially reprinted from Heydari's paper, shows values attempted in other studies and provided guidance for the method used here (Heydari, 2015). Prepared powders were weighed such that produced samples were at least 3mm thick. After a graphite foil cylinder was carefully loaded into the die using a 19.73mm plug gauge, a punch was loaded in one end and the combination of the single

punch and die were set on some 15mm stilts to hold the assembly in place for loading. A single graphite foil disc was loaded into the die after which powder was carefully poured in. The plug gauge was used again in order to compact the powders. Careful removal of the plug gauge was followed by insertion of a graphite foil disc and the second punch. The setup was then laid on its side and the punches were centered such that the sample was nearest to the pyrometer hole on the die. The assembly was then inserted into the rolled wool sleeve and the pyrometer aligned with the hole in the side of the sleeve. This whole assembly of punch, die, graphite foil, graphite wool sleeve, and sample material was taken to the furnace. A graphite cold-ram spacer was loaded onto the static (bottom) anvil, and a graphite sintering spacer loaded onto the top of that, with the aforementioned assembly then loaded on top of that. A sintering spacer and the top cold ram were placed on top of the assembly, and the top piston ram was lowered putting the sample under 5MPa of holding pressure. Pressure was then released and the assembly was aligned with the pyrometer so the pyrometer aiming reticle was aimed down towards the bottom of the pyrometer hold in the die. Pressure was reapplied, the door shut, and the SPS chamber put under a vacuum. The SPS system was then reduced to $2x10^{-2}$ torr before being backfilled with argon gas between atmospheric pressure and 1psi. The relevant program for operation was then loaded into the iTools software package, the SpecView monitoring software, and the LFM module monitor started. Figure 4 shows the iTools programming interface for setting processing parameters. Figure 5 shows the particular readouts for SpecView. This readout is typically displayed live in 1 second intervals.

Table 2 - Processing Table Listing Baseline Data on B4C-TiB2 Composites

Raw Material	TiB2 Content (vol%)	Sintering Temperature, Pressure, and time (°C, MPa, min)	Method	Strength (MPa)	Fracture Toughness (MPa*m1/2)	Hardness (GPa)	Reference
B4C, TiB2	20	1760, 40, 5	SPS	-	5.3	32.5	(Uygun, 2011)
B4C, TiB2	20	2000, 60, 6	SPS	-	3.2	32.5	(Huang, 2011)
B4C, TiB2	40	2000, 60, 6	SPS	-	4.4	30.5	(Huang, 2011)
B4C, TiB2	24	2000, 20, -	Hot Press	430.5	5.7	-	(McCuiston, 2007)
B4C, TiB2	20	2150, -, -	Pressureless	320	2.9	29	(Baharvandi, 2006)

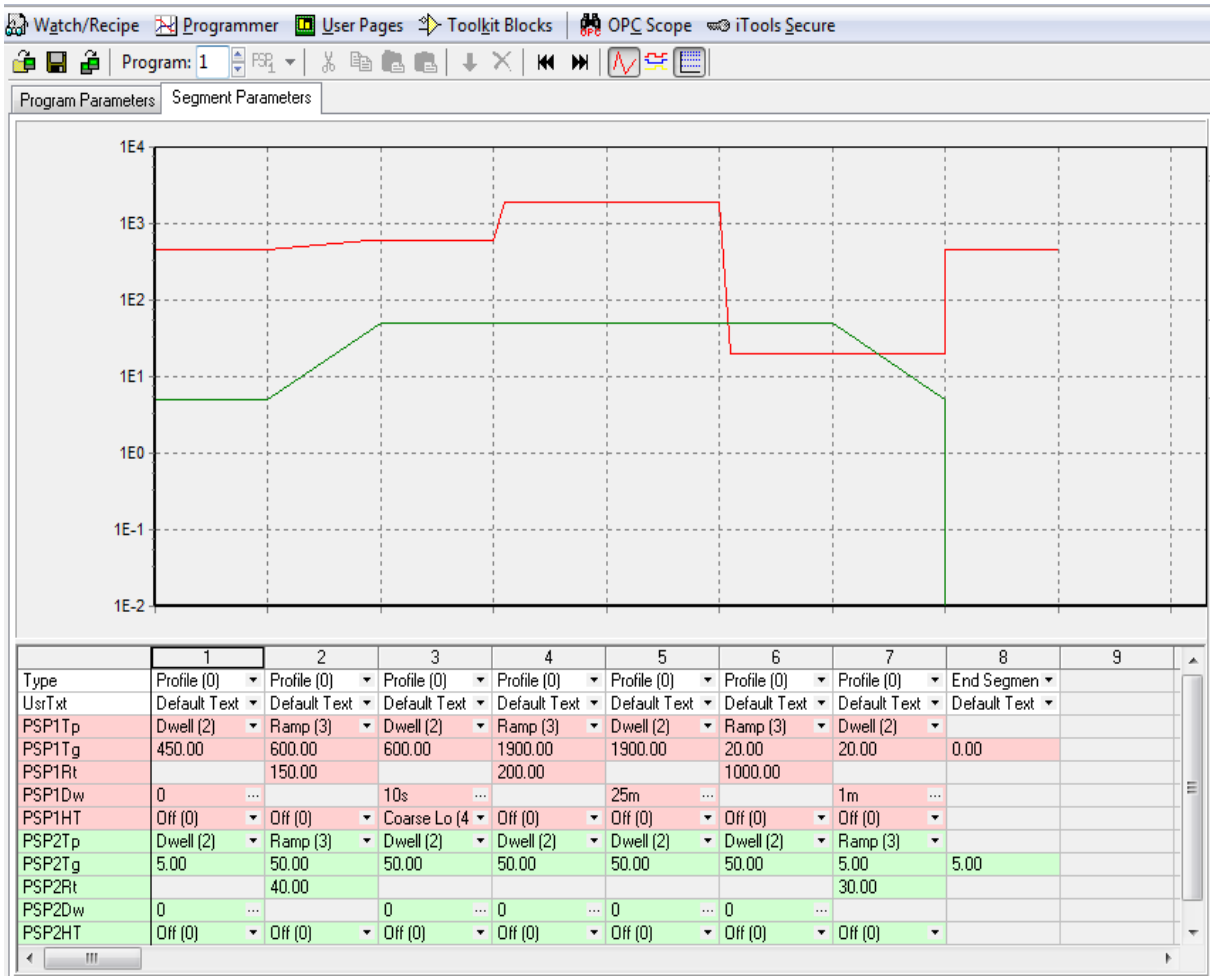

Figure 4 - iTools Interface

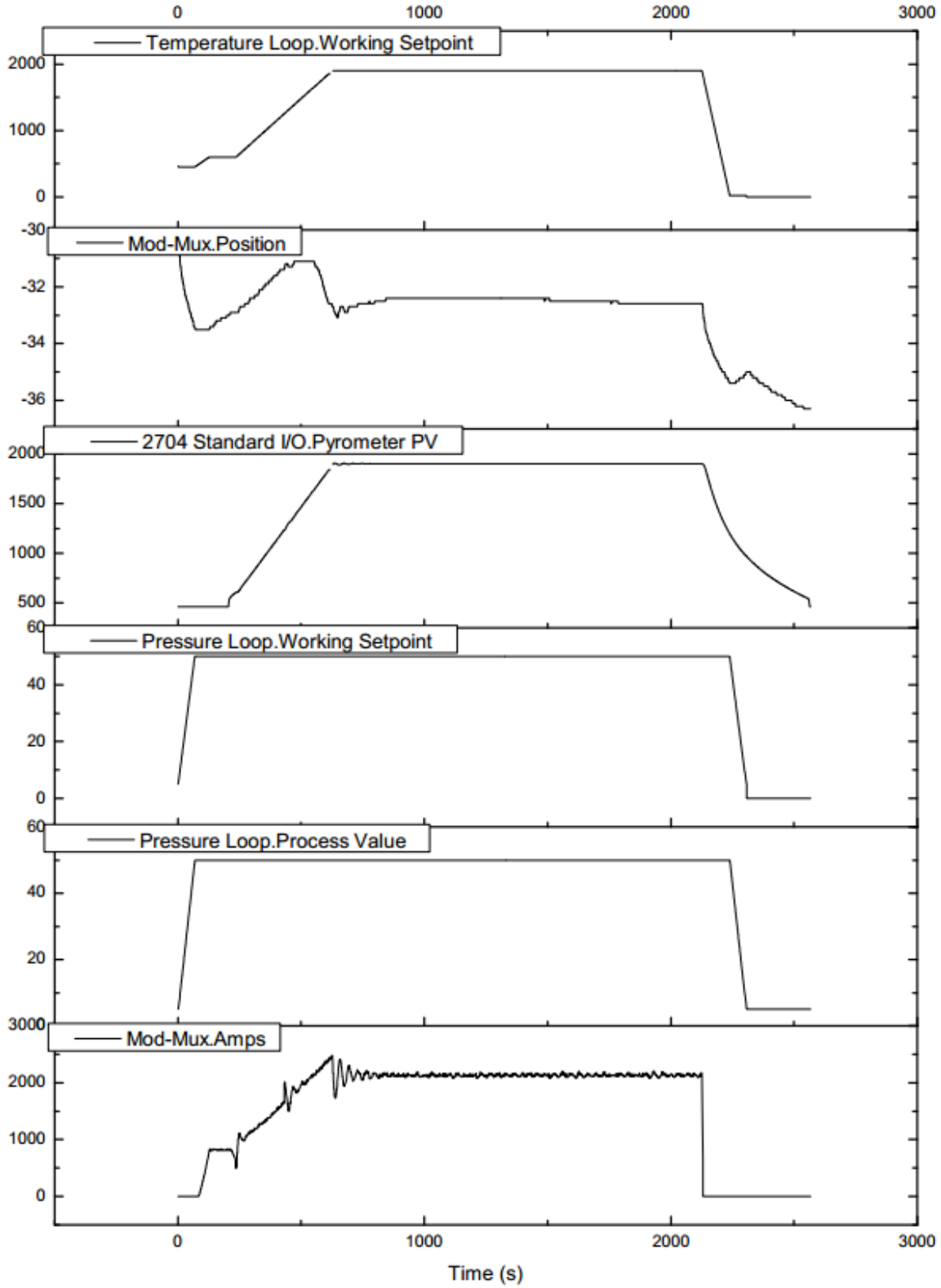

Figure 5 - Spectools Readout

After starting the program, regular observation and adjustment is required for maintaining pyrometer alignment. At program completion, the furnace is allowed to cool to near room temperature and the sample assembly is extracted. The punch and die assembly is removed, and one protruding die is carefully inserted into another die or between the jaws of a vice. The 19.73mm through hole gauge and a soft faced hammer is then used to extract the sample from its die. The loose graphite foil is picked off and the sample is carefully removed from the two punches. This process may not be trivial depending on the material and its tendency to bond to the graphite, thus some force may be necessary to remove the sample.

3.2 Machining and Polishing

3.2.1 Machining Equipment and Methodology

The process of machining and polishing was a time consuming activity in this study. Not only were many parts of testing required following fairly tight standards for comparison, but certain levels of attention to detail were required to ensure quality of characterization data. Discussed herein are the equipment, material, and consumables involved in this process.

In order to prepare finished samples for imaging, testing, and characterization, samples were machined dependent on geometric and or finishing requirements. Machining of the samples was done in the laboratory or by 3rd party machinists. Samples cut in-house were cut on a Mitsubishi FX-10 Electrical Discharge Machining (EDM) machine or a MTI Corp. STX-202 diamond wire saw. The EDM machine uses a high current discharge applied through a 0.25mm brass wire to machine samples by melting and

vaporization via dielectric breakdown between the anode and cathode. This process typically only works with materials that are conductive. In the case of B4C, we were unable to utilize Wire EDM so we instead used a diamond wire saw or shipped the samples out for machining. The diamond wire saw uses a ⌀0.30 mm steel wire coated with diamonds which mechanically abrades the sample. However with the TiB2 composites, the increased conductivity of the samples allowed for use of the EDM which is generally much more precise.

Cutting samples with the Wire EDM involved parallel and square mounting of the samples before running a basic Computer Aided Machining (CAM) tool path that the system would follow. Careful measurement of the samples and tool path were required for cutting bar samples such that the sample was cut evenly down the middle. Operation of the diamond wire saw was much simpler. Samples were mounted with hot wax on a graphite plate, and the platen's rate of ascension was slowed to 0.05mm/m to ensure the wire was not damaged in use.

Samples for mechanical testing were initially flattened on the 260μm dia-grid pad to ensure clean mounting in the EDM. Mounted samples were cut to ASTM type B geometry or the best approximation thereof for shorter samples. After cutting, preparation of machined bar samples utilized only the Dia-Grid pads beginning with the 125μm pads and ending with the 15μm pads. The 125μm pad was used to remove material to within 100μm of the final dimension and roughly within 50μm of parallelization over the 18mm span. The 70μm pad was used to get within 50μm of final dimension and 20μm of parallelization. The 30μm pad was used to get within 25μm of final dimension and 10μm of parallelization. Finally the 15μm pad was used to get within 5μm of final dimensions and parallelization. A

Mitutoyo Friction Thimble Micrometer, accurate to 0.001mm, was used throughout the polishing process to measure progress and dimensions. Although the ASTM standard did not state explicit requirements for parallelism, our samples fell under 5μm per 18mm or 10μm per 45mm of bar length. Standards for dimensions were 3 or 4 mm, with a tolerance of 0.13mm. Surface finish, as defined by the standard, was to be 600 grit or equivalent to reduce statistical error. Since 15μm is equivalent to 1200 grit, our surface finish was more than adequate. For pure B4C bar samples, due to issues from third party machining flaws, 0.5mm radius rounded chamfers were put on the long edges, and the relevant corrective factor, listed in the ASTM standard (C1161-18), was applied for subsequent stress calculations.

3.2.2 Polishing Equipment and Methodology

Polishing of samples was done primarily on polishing wheels made by Allied High Tech (AHT). The Multiprep auto-polishers were used extensively for facing the surfaces of the samples fresh out of the SPS system. Dia-Grid pads, from AHT, were required to machine the samples as no other conventional material was suitable for this process given the hardness of B4C. These dia-grid pads were of diamond sizes 260μm, 125μm, 70μm, 30μm, and 15μm. Fine polishing was carried out on AHT White label polishing pads using polycrystalline diamond pastes. Pastes of diamond sizes 6μm, 3μm, 1μm, 0.25μm, and 0.05μm were used. Final finishing was done on a Buehler Vibromet in 0.04μm colloidal silica.

For imaging purposes and hardness testing purposes, samples were mounted to a parallel polishing fixture for an Allied High Tech Tech-Prep auto-polishing system. The

parallel fixture was then leveled against the platen, and the sample was ground flat with Dia-grid Nickel-Bonded Diamond polishing pads, using a constant flow of water to flush polishing debris and act as a lubricant. Beginning with the 260μm diamond pad, and proceeding through 125μm, 70μm, 30μm, and 15μm pads. Once flattened by the 260μm pad, each successive pad was used for 15 minutes on the auto-polisher, utilizing oscillation and rotation and the maximum available weight of approximately 500g. After the 15μm pad, the sample was polished on AHT Dia-Mat or White Label pads using polycrystalline diamond paste. The progression for these pads was 6μm, 3μm, 1μm, 0.25μm, and 0.05μm and hexylene glycol (AHT Green Lube) was used as a lubricant sparingly. Between each of these pads, the sample was ultrasonically cleaned for 5 minutes in dilute Valconox Liquinox detergent, rinsed with distilled water, and ultrasonically cleaned in methanol for 1 minute before drying with compressed air and moving to the next pad. The final step in polishing for the samples was 24 hours on the Buehler vibratory polisher in a solution of 0.04μm colloidal silica.

Cleaning of the polished samples after the colloidal silica polish was important to remove any crystallized agglomerates of silica. Samples were cleaned in dilute detergent at a temperature of 50C for half an hour, then in methanol for 15m at room temperature to ensure totally clean surfaces. The density of the samples was measured using the Archimedes principle/method in distilled water (ASTM B962-17), and verification of the Archimedes method was done with sample fragments in a Micrometrics Accupyc II gas Pycnometer.

3.3 Microstructural Characterization

3.3.1 Imaging and Analysis

Scanning electron microscopy was carried out on an FEI Quanta ESEM and NOVA Nano-SEM. The purpose of the microscopy was to characterize and quantify grain size and distribution of phases in each of the composites. It was also important after fracture strength testing (described in section 4.5) to examine the fracture surfaces for morphology and fractography. Samples to be examined under SEM were polished and cleaned according to methods explained above before being mounted to SEM stubs using conductive carbon tape. Images were taken at several magnifications before being analyzed. In addition, an EDAX® energy dispersive X-ray spectrometer (EDS) was used during SEM imaging to determine elemental composition.

ImageJ, a publicly available image processing and analysis program, was used primarily to quantify the area and volume fractions of the composite phases, the grain size analysis on highly polished samples, and fractographic studies.

Grain size analysis was accomplished through contrast based differentiation between grains of B4C and TiB2, as well as between different crystallographically oriented grains of pure B4C in highly polished samples. Analysis of pure B4C Grain sizes was done by manually identifying grain boundaries in a 3250x magnification micrograph, then reducing any grayscale such that only the boundaries remained. Residual imperfections from imaging were also manually removed before the individual grains were analyzed. Analysis of composite samples followed the same procedure for the B4C portions while for TiB2, due to Z-contrast, were isolated and computed separately from the B4C.

3.3.2 X-Ray Diffraction

X-ray diffraction (XRD) was carried out on a Rigaku Ultima III X-Ray diffractometer equipped with a Cu-Kα with wavelength 0.15418nm. Operating voltage was 40kV and operating current was 33mA. The diffraction experiments were performed over a 2θ of 20 to 90 degrees. The sample step size for all experiments was 0.10 degrees per minute while scanning speed varied between 2.3 and 4.7 degrees a minute depending on use case. The selection slit was 5 degrees, divergence height limiting slit was 2mm, and the receiving sit was 5 degrees.

The purpose of the XRD was analysis of the composite phases, verification of the crystal structures, and internal stress factors in the composite materials. XRD was performed on the powders, before and after mixing, and on the monolithic composites. Finely polished and cleaned samples were used to ensure graphite contamination was not present in pores and pits. Powder samples were loaded in a small square die and placed on glass slides. Powder thickness was approximately 2mm for the purposes of crystal structure verification, 15 minute scans were used, scanning at 4.6 degrees a minute.

When higher resolution was needed for internal stress identification, sintered samples of thicknesses between 3 and 4mm were centered on the platform and scanned at, 2.3 degrees a minute. This significantly resolved peak shifting due to the stress states from mismatched coefficients of thermal expansion.

The Jade 9 software package was used for analysis of the XRD diffraction plots to resolve the crystallographic peaks, peak shifting, and identify elemental presences. After importing the raw data, it was necessary to include all elements expected to be present. In

the case of the milled powders, for example, checks were made for cobalt and tungsten. For the sintered samples, checks were made for elemental graphite contamination.

3.3.3 Synchrotron High Energy X-Ray Diffraction

This study benefitted from the opportunity to perform a few synchrotron radiation x-ray diffraction (SR-XRD) analyses which proved critical in verifying both our composition, due to deviation from the mass fraction inputs, and verifying stresses through the bulk of our samples. Compared to the use of standard XRD on the Rigaku, which uses Copper Kα radiation of approximately 8eV, SR-XRD uses much higher energy radiation that permits the full penetration of the test samples, approximately 3mm thick.

SR-XRD data was collected at the Advanced Photon-Source at Argonne National Laboratories in the Sector 6-ID-D Beamline using the transmission mode. Diffraction patterns were performed using a monochromatic 65keV (wavelength of 0.0192040 nm) X-Ray Beam with a beam size of 200μm by 200μm. Exposure was approximately 0.1 seconds and averaged over 100 exposures. Each sample was positioned and centered on the beam. Data collection was done with a Perkin Elmers amorphous silicon detector positioned behind the beam-stop about 75cm from the sample. Calibration of the detector was performed with the standard Cerium Oxide (CeO2) powder. The intent was to collect Debye-Scherrer diffraction patterns like those for standard XRD that allow for identification of the crystal structure of the material and its potential stress states. Data analysis was done with Fit2D (Hammersley, 1996) to resolve the patterns and stress states. Calculation of the compositional fraction was done by correlation of the collected data against nominal powder diffraction files for pure TiB2 and B4C. Analysis of the data and

comparison with the powder diffraction patterns of the pure materials allowed for quantitative definition of the actual volume fraction of the B4C and TiB2.

3.4 Mechanical Testing

Mechanical testing was an important step for comparative analysis with prior experiments from the literature. ASTM standards were followed as closely as possible where applicable. All local testing of bar samples for fracture strength was carried out on an Instron 8872 load frame with a 1kN load cell and 3-point bend testing apparatus. Hardness testing with the Vickers micro-hardness testing system followed standard procedures.

3.4.1 Vickers Microhardness

Highly polished samples were placed on the testing platen and locations were verified in the attached microscope. The test was started with a 1kN load and 10 second dwell. When the test was completed, the indent was identified and the dimensions of the indent were measured. If the indents were comparatively irregular due to chipping out, the data was ignored and an additional test performed. The Vickers hardness at the 1kN load also generated cracks at the corners of the indents, and these crack lengths were used to estimate fracture toughness through well-known empirical equations, such as Equation 1(Niihara, 1983):

$$K_c = 0.016 \sqrt{\frac{E}{H}} * \frac{P}{c^{1.5}}$$

Equation 1. Fracture Toughness Estimation

where K_c is the critical stress intensity factor, better known as fracture toughness, E is the elastic modulus, H is the hardness, P is the applied load, and c is the crack length. Geometrical effects and other terms are combined into the dimensionless calibration constant 0.016 (Quin, 2007). The values are relative since the stress intensity factor is not being measured and future studies will implement Chevron-notches followed by three-point bend testing to better quantify fracture toughness.

3.4.2 3-Point Flexure Strength Testing

The bar samples were loaded onto the 3-point bend test apparatus for the Instron load frame. The test was carried out in accordance with the ASTM C1161-13 standard at a crosshead speed of 0.5 mm/min until a preload of 10N was registered. A 3-point spacer width of 16mm was used for 20mm samples, and a spacer width of 40mm was used for 45mm samples. An image of the test setup is shown in Figure 6. Samples were individually measured by thimble micrometer to 0.001 mm for each test, then manually centered and squared in the testing apparatus with a small 1" gauge block and an adjustment micrometer on the testing apparatus. In the case of samples with chips, visually identified in a 10x stereo microscope, the damaged sides were oriented up to reduce their effect on the final results. Instron's Bluehill software was used to control the load frame and a programmed method was used for each specific geometry tested. The test was started and the load frame advanced the head to apply a preload briefly before beginning the actual test (ASTM C1161-18). The bend (flexural) strength, S, was determined using Equation 2, where P is the breaking force, L is the outer support span of the fixture, b is the specimen width, and h is the specimen thickness. After the samples fractured, the two pieces were

gathered before beginning the process with the next bar. At least four bars were tested for each composition.

$$S = \frac{3PL}{3bh^2}$$

Equation 2. Flexure Stress from Geometry and Breaking Force

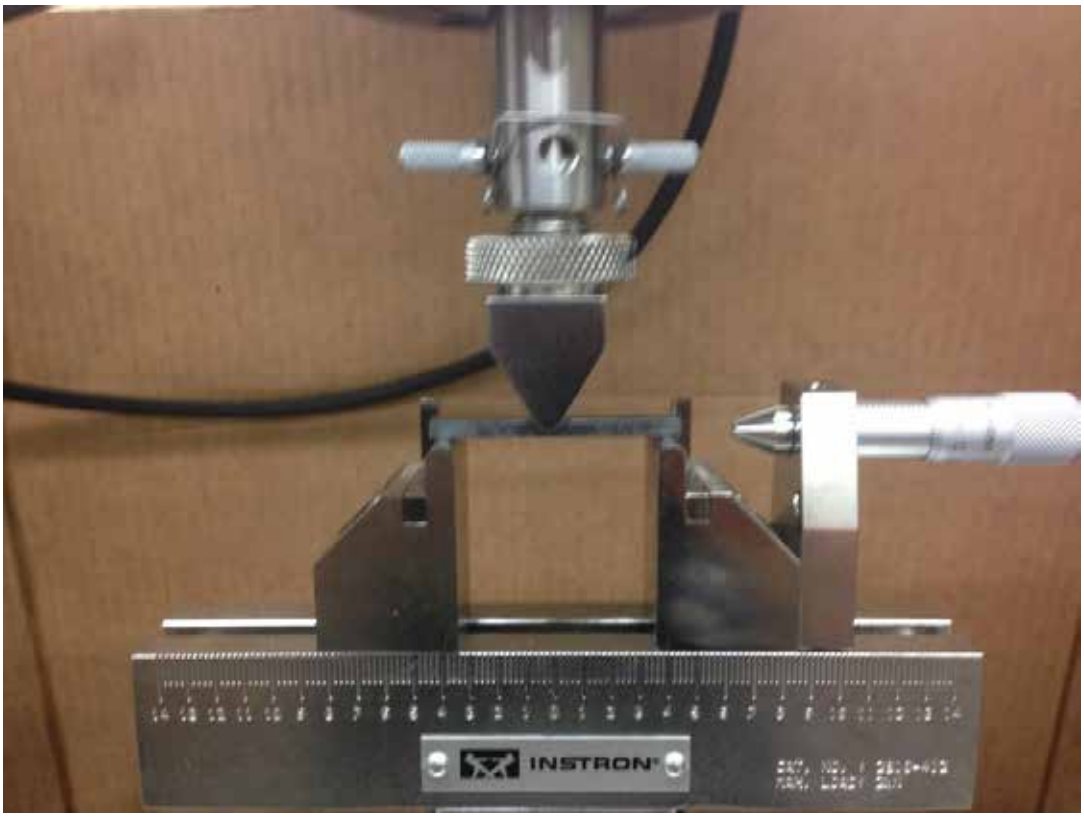

Figure 6 - Instron 3-Point Test Apparatus

CHAPTER 4

RESULTS AND DISCUSSION

4.1 Microstructure

4.1.1 Grain Size and Morphology

4.1.1.1 Pure B4C and B4C-TiB2 Composites

In Pure B4C, the starting powders were of unquantified size distribution, and the manufacturers had no powder size distributions however sizes were listed on the assay as under 3μm. Considering this and the 3rd order polynomial fit of the grain size distribution data, there is a definite peak in grain sizes around the stated 3μm mark. There is also evidence of abnormal grain growth noted in the literature with the non-normal distribution of grain sizes at the upper end of the histogram. Analysis of the grain size distributions is shown below in Figures 7, 8, and 9.

While B4C does not appear to experience excessive grain growth or Ostwald ripening, TiB2 does. The size of the starting powder and its resultant aggregation and growth is evident in the composite micrographs. Figure 7 and Figure 10 show the grain size distribution and identification for a pure B4C sample with a mean diameter of 4.29um, a standard deviation of 3.77um, and a median grain diameter (D50) of 3.56um. The irregular grain growth (Basu, 2006) is clearer here with the relatively high standard deviation.

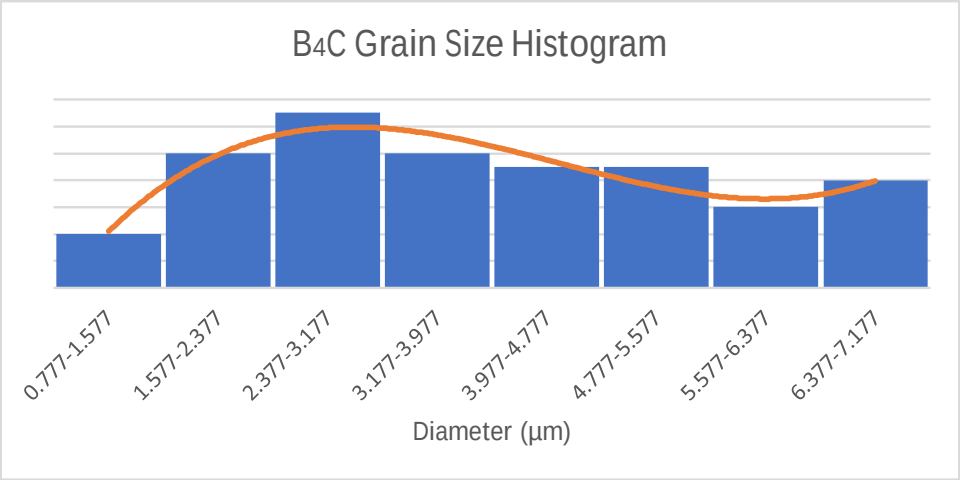

Figure 7 - B4C Grain Size Distribution Histogram

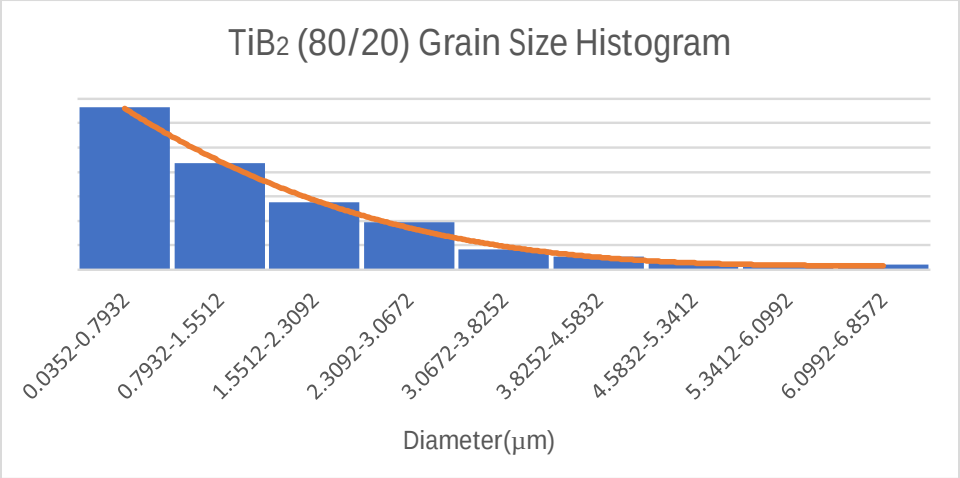

Figure 8 - 20% (Volume % powder) TiB2 - Grain Size Distribution Histogram

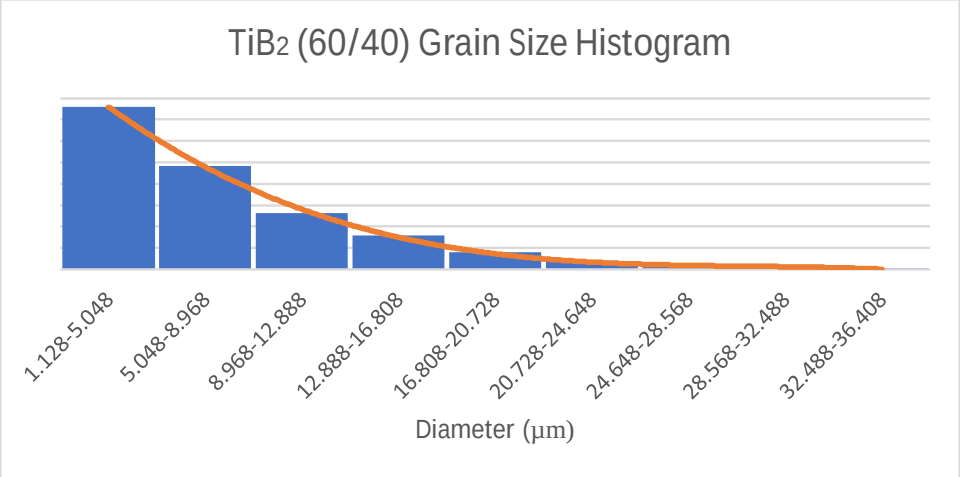

Figure 9 - 40% (Volume % powder) TiB2 - Grain Size Distribution Histogram

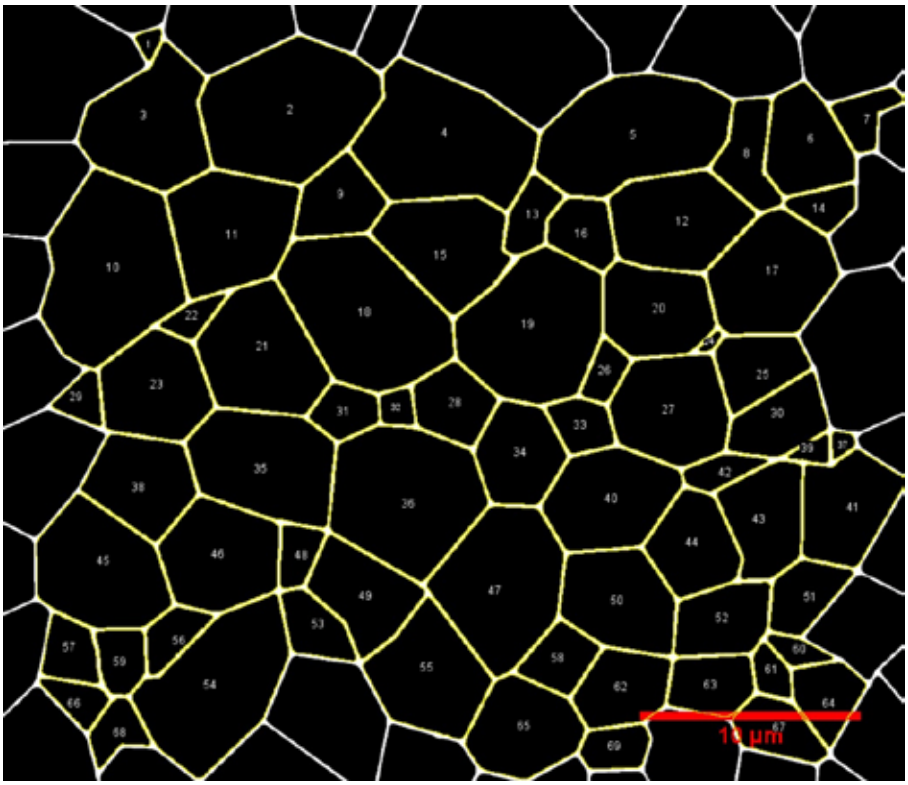

Figure 10 - ImageJ Grain Identification for Pure B4C

4.1.1.2 B4C and TiB2 Grain Distribution in the Composite

Homogenization of the composite structure was done through powder processing. Powders were rolled for 24 hours, and Figure 11 shows the comparison between 2 and 24 hours of rolling on the homogenization of the TiB2 and B4C. It is clear in the 2-hr sample that the distribution of the TiB2 is much more varied than that of the 24-hr sample. Due to the tendency for TiB2 to experience excessive grain growth, the size and morphology of the TiB2 is not unexpected (Basu, 2006). Despite this tendency, it is beneficial to the microstructure that these aggregates are the size that they are. Given their size and shape they work well for the purposes of crack deflection. It would be worth looking into the difference between finer and more homogeneous distributions of particles in this particular composition. The quantification of this could be easily calculated by hand on

fracture surfaces with a linear system in the case of Figure 12 where the red line is a rough trace of the fracture, and the blue line is a linear approximation. Mapping of the surface of a fractured bar could also prove to be more precise, comparing it against that of a flat plane or simple conchoidal fracture plane model.

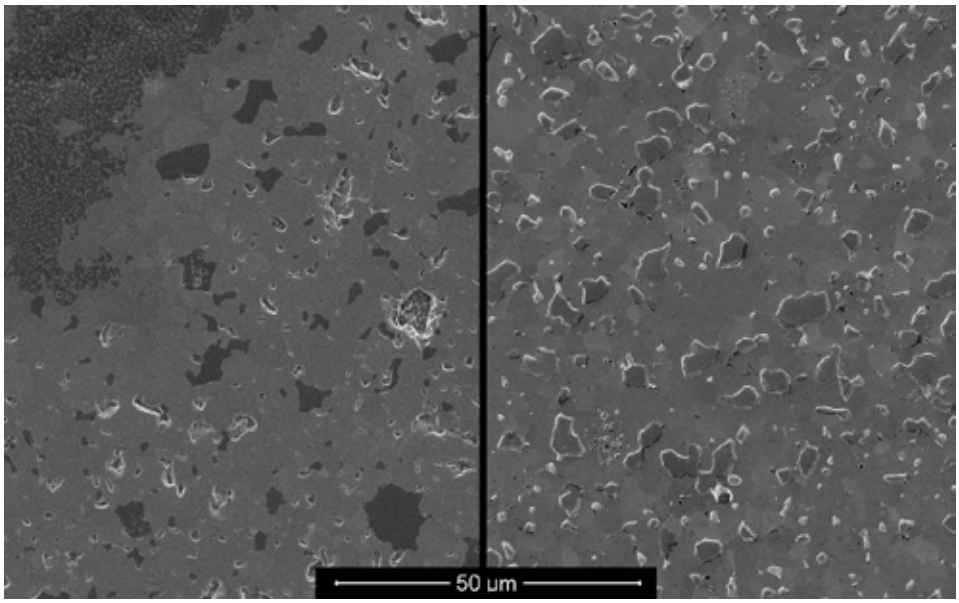

Figure 11 – 2Hr Rolled vs 24Hr Rolled 40%-TiB2

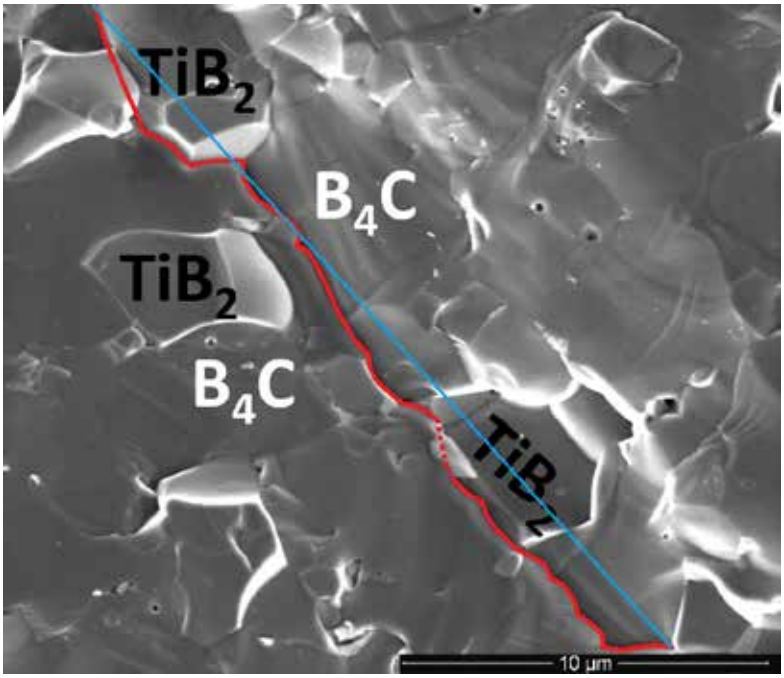

Figure 12 - Comparing Real (Red) vs Linear (Blue) Crack Lengths

4.1.1.3 Anomalous Deviations in Density

Measured densities of the samples, verified through image analysis of polished samples and synchrotron diffraction, did not match the input mass fractions. Examination of the thermodynamics with Fact-Web's equilibrium calculations implied that manufactured powders assays may have been incomplete or inaccurate. Adding to the complication is the likely presence of B13C2 (Bullett, 1982) which is a common byproduct of B4C synthesis. In analysis of XRD, the close relationship between B4C and B13C2 makes the two somewhat difficult to differentiate at first. It is likely that B2O3 on the B4C Powders, the B2O3 and TiO2 powders on the TiB2, and the excess boron from the B13C2, could react with the powders and graphitic die materials. At low pressures and high temperatures, the $B2O3_{(gas)}$ from both the powders will dissociate and in combination with the excess boron will react with the graphite of the shielding graphite foils and dies to produce more B4C. Table 3 shows the mass fractions input, the density according to the input, the volume fractions calculated by synchrotron and image analysis, and the recalculated densities. With samples that were made with 60% B4C and 40% TiB2 (as starting powder feedstock volume percent), the ultimate volume fraction ended up being around 77% B4C and 23% TiB2. Analysis in Fact-Web (Bale, 2016) showed that the TiB2 is much more stable. This is reproduced in Table 4 showing free oxygen from the decomposition of boron oxide does not result in any change to the TiB2, instead reacting with the graphite in the tooling. This is correlated with its free energy of formation compared against that of B4C and TiB2. Based on this, it is assumed that the reactive synthesis of B4C is the reason for this change in B4C volume fraction. Solving for the requisite excess boron to account for this change would require more than twice the initial

input mass of B4C. If the additional boron is present in the raw powders then some additional reactive mass must come from the punches dies and foil. Quantification of the loss in mass in the punches and dies however might be quantifiable given the gain in mass is substantial. Looking again at Table 4 there is a loss in graphite and an increase in B4C which supports the conversion of surface oxides to B4C. Additional studies with X-Ray Photoelectron Spectroscopy or possibly Fourier Transform Infrared Spectroscopy could be done on the raw powders or pressed green compacts to determine some of the superficial bonding. More complex thermodynamic studies of the system would be important in understanding the root cause of this density discrepancy.

Table 3 - Mass Fraction Table

Mass Fraction Input		Percent Density	M-F from Images		M-F from Synchrotron		Recalculated Density
B4C	TiB2		B4C	TiB2	B4C	TiB2	
100	0	100	100	0	100	0	<99
80	20	90	84	16	86	14	<99
60	40	94	77	23	77	23	<99

Table 4 - TiB2 Stability at Standard Processing Temperatures, Varying Pressures

2173K **1atm**			2173K **250atm**		
Input (moles):			Input (moles):		
0.01 B2O3 + C + 0.05 B4C + 0.04 TiB2			0.01 B2O3 + C + 0.05 B4C + 0.04 TiB2		
Output (moles):			Output (moles):		
3.00 mol		Gas	Effectively 0		Gas
99.74%	CO				
0.14%	BO				
0.11%	$(BO)_2$				
0.97	C	Solid	0.01	B_2O_3	Liquid
0.055	B_4C	Solid	1	C	Solid
0.04	TiB_2	Solid	0.05	B_4C	Solid
			0.04	TiB_2	Solid

Figure 12 shows SEM images and corresponding ImageJ images of 40% TiB2 loading (23 vol.% TiB2) of UNT and scaled-up QCML composites. It is evident there is a relatively homogeneous distribution of TiB2 secondary phase in the B4C matrix with no residual carbon. Both UNT and scaled-up QCML samples show similar area fractions of TiB2 based on numerous ImageJ analyses of both 20% and 40% loadings. For consistency, mass fractions will be maintained when referring to samples rather than the post analysis volume fractions.

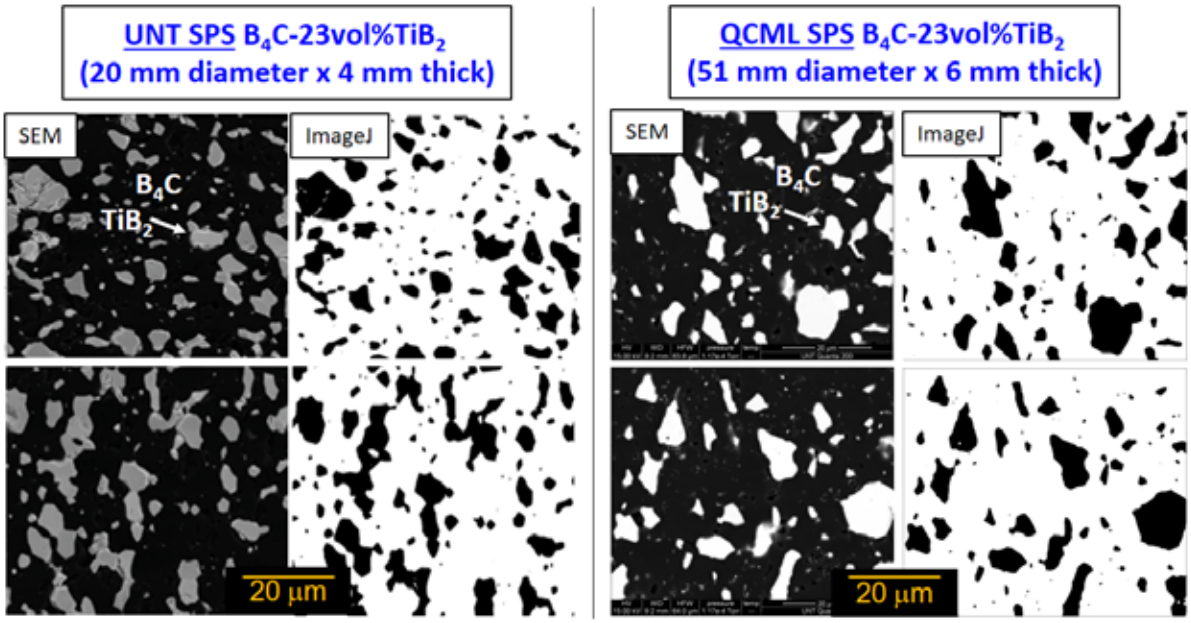

Figure 13 - Equivalent TiB2 Loading for 40% Mass Fraction Input For UNT and QCML Composites

4.1.2 Internal Residual Stresses

4.1.2.1 XRD

Figure 13 shows XRD scans of a continuum distribution of B4C and TiB2 in 20% increments (volume fraction of starting powder feedstock). An apparent shift in 2θ (d-spacing) is evident as the composition moves towards the eutectic. The primary limit of

this study is the superficial nature of low energy XRD. The analysis depth of the Cu-Kα radiation is typically around 3λ, or about 0.46nm. This naturally depends on the absorption coefficients, packing fraction, and specific gravity.

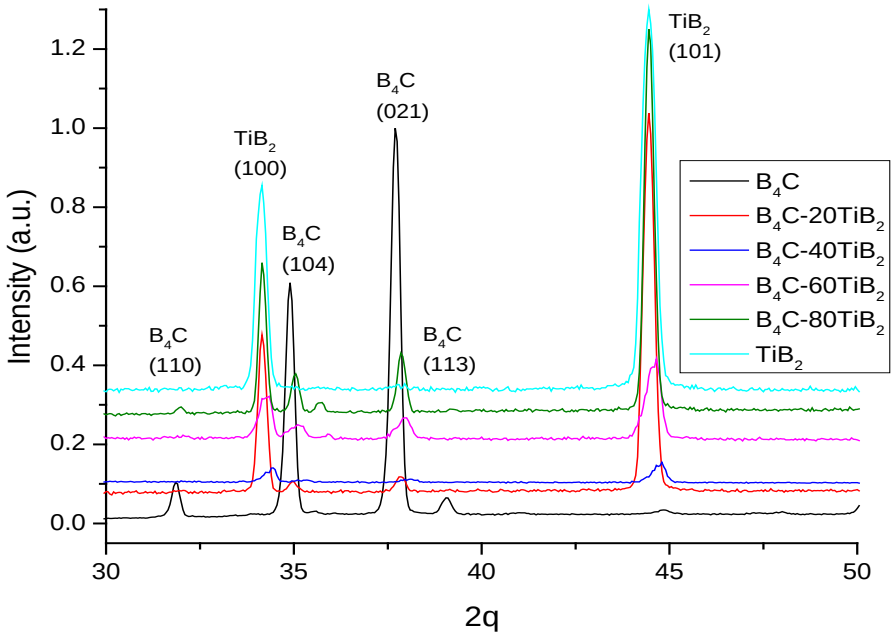

Figure 14 - XRD Plot of Compositional Gradient in B4C and TiB2

4.1.2.2 Synchrotron XRD

Synchrotron studies were performed at Argonne National Laboratories for several purposes. The quantification of the sample compositions, which was only statistically verified by the ImageJ analysis, was finally done with the high energy X-ray diffraction. The analysis and verification of residual stress states from differing coefficients of thermal expansion was also verified against the XRD plots. The use of synchrotron X-rays also allowed for the bulk analysis of the material's internal stresses, where XRD only effectively analyzed the surface of the samples studied.

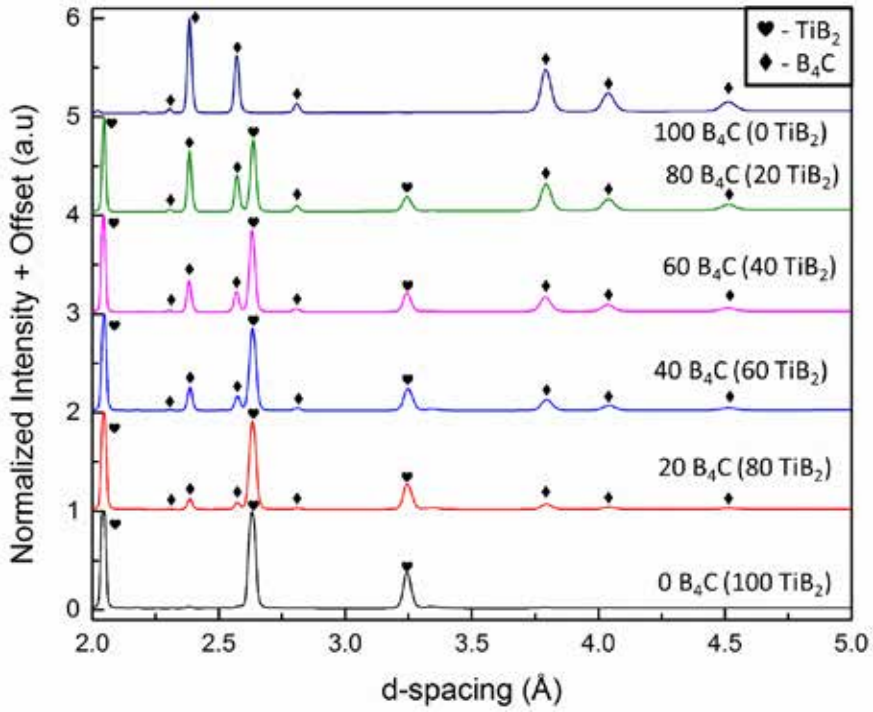

Figure 15 - Synchrotron Diffraction of B4C-TiB2 Compositional Gradient

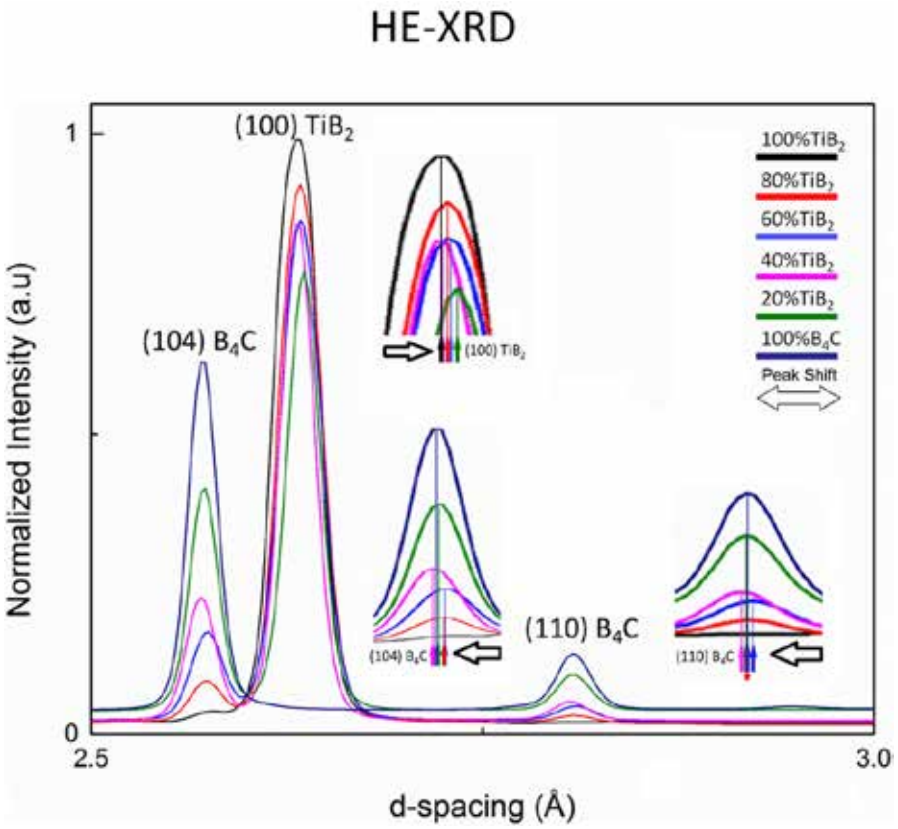

Figure 16 - Zoomed in Region of HE-XRD of B4C-TiB2 Compositional Gradient

An examination of the internal stresses, as in the Figures 14, 15, and 16 XRD plots, can be seen in the peak shifts. The shifting of the peaks is a result of stresses on the lattice. Peak shifts indicate compressive behavior for B4C (decreasing d-spacing) and tensile behavior for TiB2 (increasing d-spacing). This is a result of thermal residual stresses between B4C matrix and TiB2 phase during cooling (DT=1875°C) due to their coefficient of thermal expansion (CTE) mismatch. The CTE for Pure B4C and TiB2 are $5.65*10^{-6}K^{-1}$ (Klam, 1987) and $7.4*10^{-6}K^{-1}$ (Lonnberg, 1988) at 20°C respectively. Since the CTE for TiB2 is higher than that of B4C, it is expected and seen here, that the TiB2 is put in a state of tension. This is especially evident looking at the first series of peaks in Figures 15 and 16. For the Highest B4C to TiB2 ratio we see the highest strain on the lattice. Likewise, as the proportion of TiB2 to B4C increases we see the strain decrease correspondingly. This will place the B4C -TiB2 boundary under tensile stress leading to interfacial micro-crack toughening mechanism (Taya, 1990).

4.2 Mechanical and Fracture Properties

4.2.1 Microhardness

Table 4 lists property values for SPS B4C, TiB2, and B4C-TiB2 composites with comparisons to armor-grade PAD B4C and PAD SiC-N literature values (Vargas-Gonzalez, 2010). Scaled-up QCML pure B4C and B4C-40%TiB2 composites property values are also listed in Table 4. All the SPS samples are ~99% theoretical density with the exception of pure TiB2 for reasons stated earlier. It is evident that a low density of $2.5g/cm^3$ is maintained for SPS B4C compared to commercial armor-grade PAD-B4C. As expected, a

slight increase in density is exhibited by the B4C-20%TiB2 and B4C-40%TiB2 composites from 2.76 to 2.99g/cm^3, respectively.

The SPS B4C and B4C-TiB2 composites were much harder than PAD B4C due to the lack of residual carbon (graphite) in the SPS samples which would otherwise weaken the material by providing stress concentrations. As expected, the hardness slightly decreased in the composites when adding more TiB2 since it is softer than B4C. Also, the hardness of scaled-up QCML SPS samples agrees well with the UNT SPS samples.

Table 5 – Properties from SPS Samples and the Literature

	Process (Manufacturer)	Density (g/cm^3)	% Theoretical Density	Vickers Hardness (GPa)	Fracture Toughness (MPa*m$^{0.5}$)	Flexural Strength (MPa)
PAD-B_4C	Hot Press (BAE)	2.5	99	26	2.9	398
PAD-SiC-N	Hot Press (BAE)	3.2	99	23	4.5	578
B_4C	SPS (UNT)	2.5	99	37	3.4	405
	SPS (QCML)	2.51	99	36	3.2	TBD
B_4C-20TiB_2	SPS (UNT)	2.76	99	35	3.7	446
B_4C-40TiB_2	SPS (UNT)	2.98	99	33	6.9	519
	SPS (QCML)	2.99	99	32	7.2	462
TiB_2	SPS (UNT)	4.41	94	28	4.5	377

4.2.2 Fracture Toughness Estimation from Vickers Indent Cracks

As explained earlier, the indentation fracture toughness is an estimation of the toughness since the stress intensity factor is not being directly measured. Future

toughness values will be quantified with Chevron notched-beam fracture toughness using the 3-point bend test. Figure 17 and Figure 18 show representative indentation-induced cracks in pure B4C and B4C-40%TiB2 composites to measure the fracture toughness based on Eqn. 1. Table 5 shows that the B4C-TiB2 composites exhibit a ~35% increase in hardness and fracture toughness compared to commercial armor-grade PAD-B4C since there is no residual graphitic carbon observed in the SPS B4C-TiB2 composite as there is in the commercial armor-grade PAD-B4C. Vickers micro-indentation revealed decreasing mechanical hardness with increasing TiB2 content although there was a large increase in fracture toughness with the increased TiB2 fraction of 40%%. This is evident by comparing the smaller crack lengths in the B4C-40%TiB2 composite. The H/Kc ratio, a measure of inelastic deformation/quasi-plasticity, that decreases with increasing TiB2, has been linked to an increase in penetration resistance. Thus, the B4C-40%TiB2 composite with a H/Kc ratio of 4.8 would be expected to exhibit increased quasi-plasticity. This was confirmed with Vickers micro-indentation of the B4C-40%TiB2 composite where the cracks are deflected around grains of B4C/TiB2 following their grain boundaries, shown in Figure 18 and Figure 19. Quasi-plasticity is desirable because it decreases the magnitude of the local stress as well as the deformation gradients that enable the load to spread over a larger volume of material. In addition to crack deflection, the TiB2 phase aids in crack bridging (also shown in Figure 18 and Figure 19). When combined with the previously discussed interfacial micro-crack toughening mechanism in the B4C-TiB2 composite, a higher toughness is clearly exhibited when adding TiB2 to B4C.

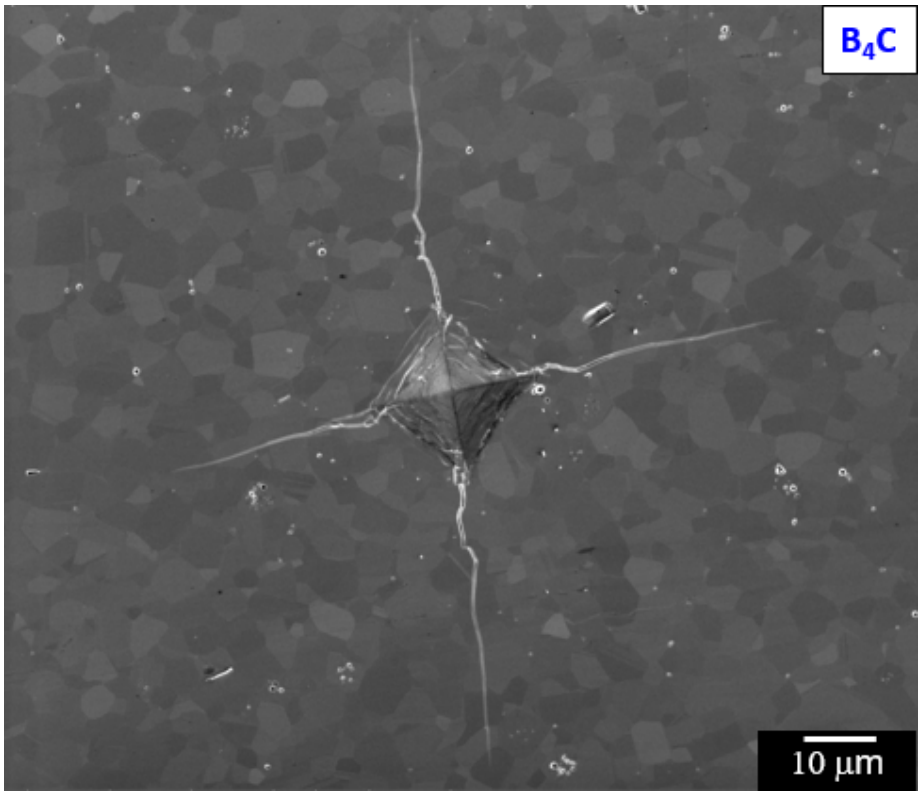

Figure 17 – SEM Image of Vickers Microhardness Indent in Pure B4C

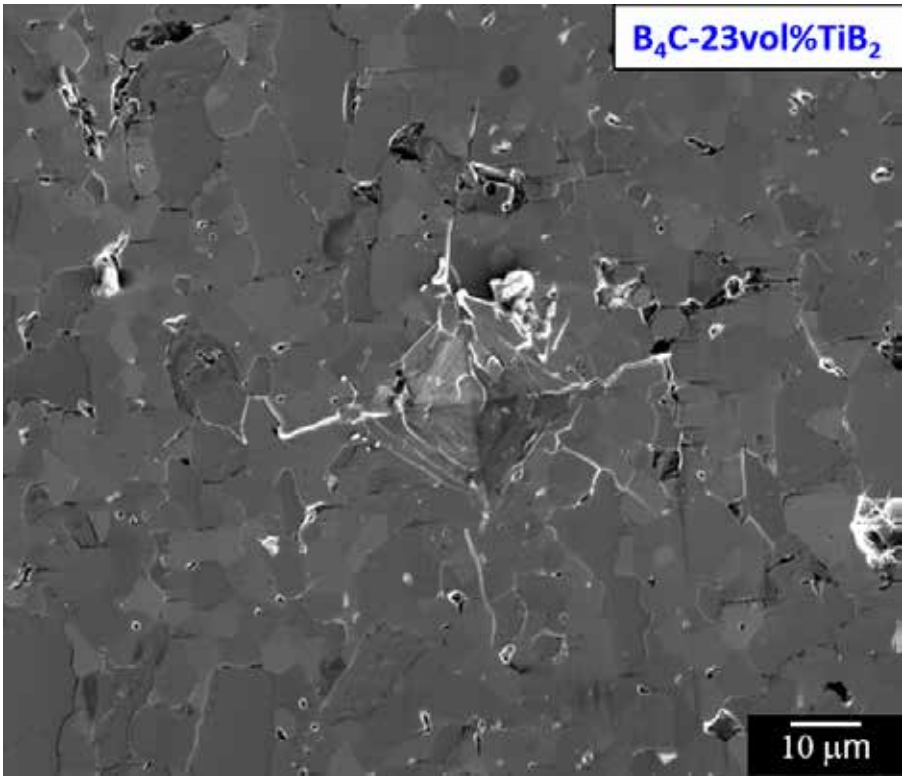

Figure 18 – SEM Image of Vickers Microhardness Indent in B4c-40%Tib2 Composite

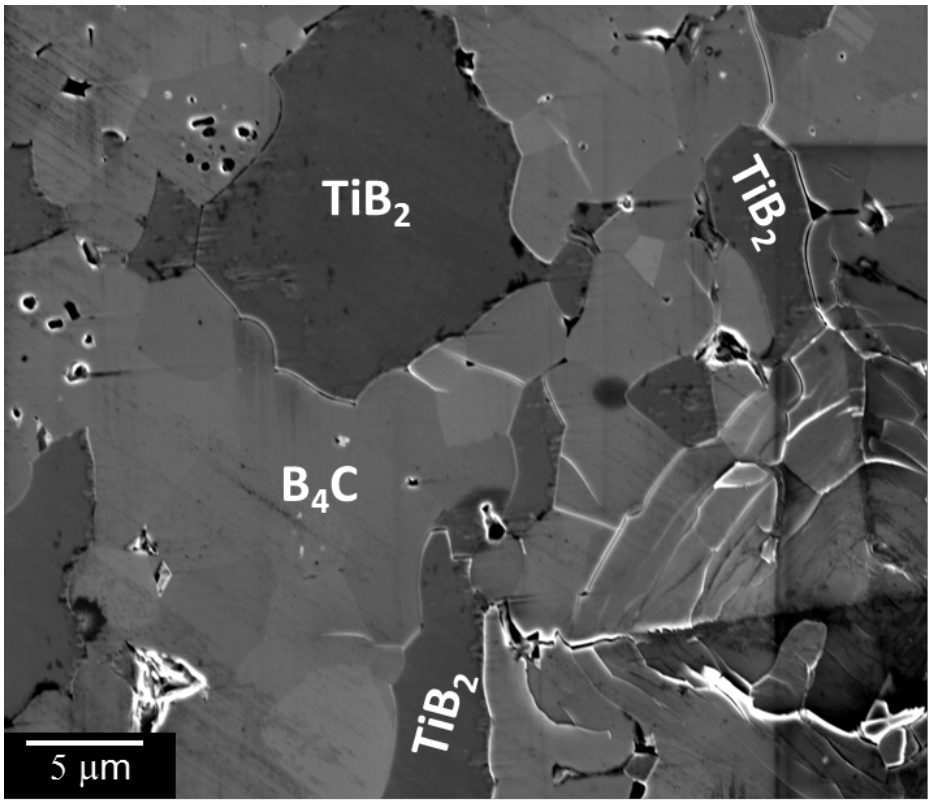

Figure 19 High Magnification SEM Image of Vickers Microhardness Indent in B4C-40%TiB2 Composite

4.2.3 Flexural (Bend) Strength

Table 5 lists the 3-point bend test flexural strengths of B4C, TiB2 and the B4C-TiB2 composites. Similar flexural strengths are exhibited between PAD B4C and SPS B4C while there is a ~30 % increase in strength in the B4C-40%TiB2 composite.

4.3 Fractography of Cleavage Surfaces

Comparisons were made between B4C and B4C-TiB2 fracture surfaces after 3-point bend testing to determine the strengthening mechanism. Figure 20 and Figure 20 show typical low and higher magnification SEM images of the fracture surfaces of SPS pure B4C, respectively. The fracture surfaces only exhibit transgranular fracture in agreement with

PAD B4C (Vargas-Gonzalez, 2010). Figure 21 shows several SEM images and an EDS map of the fracture surfaces of B4C-40%TiB2 composite. In contrast to pure B4C, the B4C–40%TiB2 fracture surfaces show mixed mode fracture – intergranular fracture occurred along the grain boundary of TiB2 phase while transgranular fracture occurred with B4C grains. The presence of TiB2 forces the microcracks to propagate in a non-planar fashion thus enhancing the energy dissipation at the crack tip. Thus, the addition of TiB2 serves as a strengthening, and previously discussed, toughening phase.

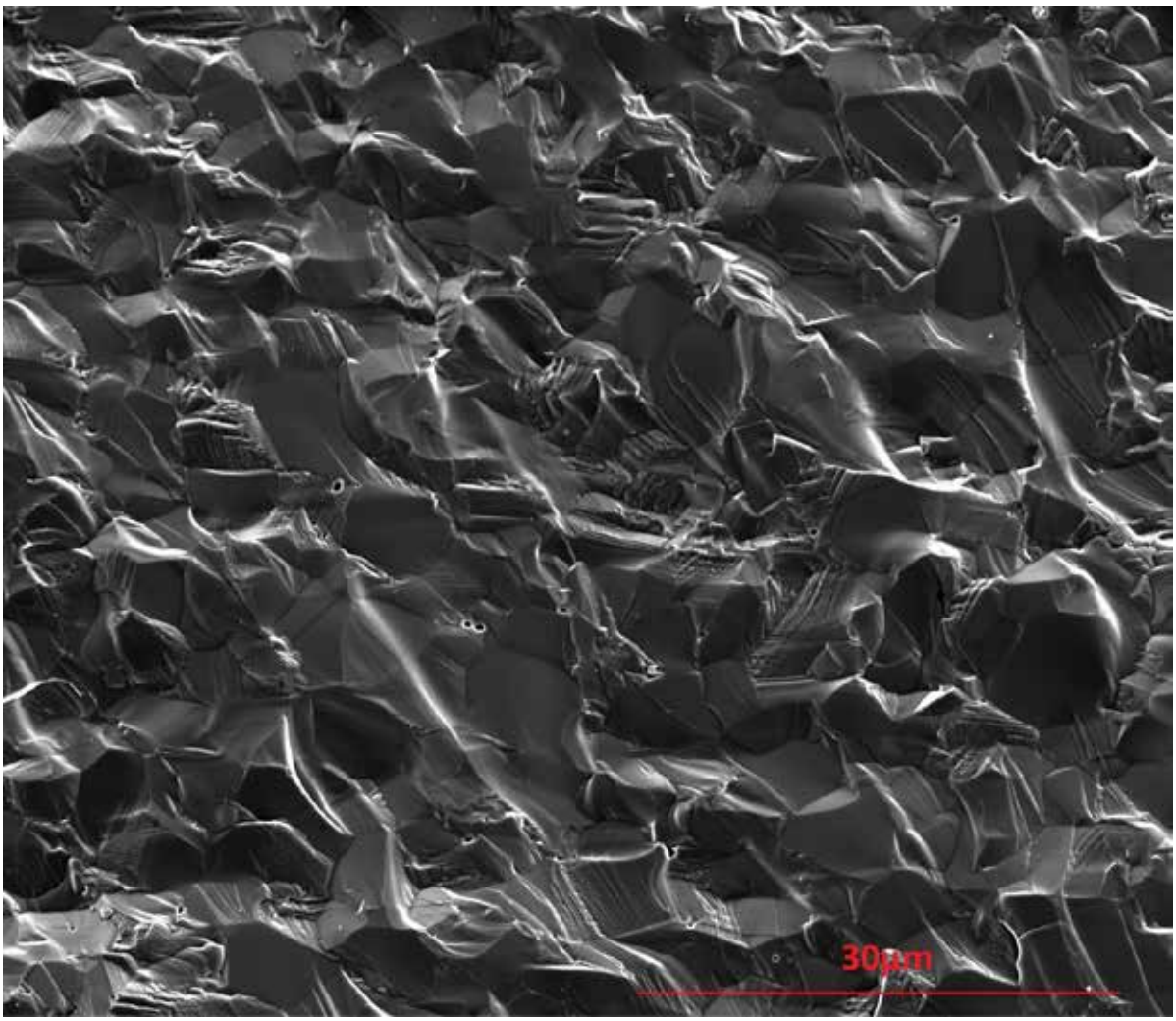

Figure 20 – Low Magnification SEM Image of B4C Fracture Surface

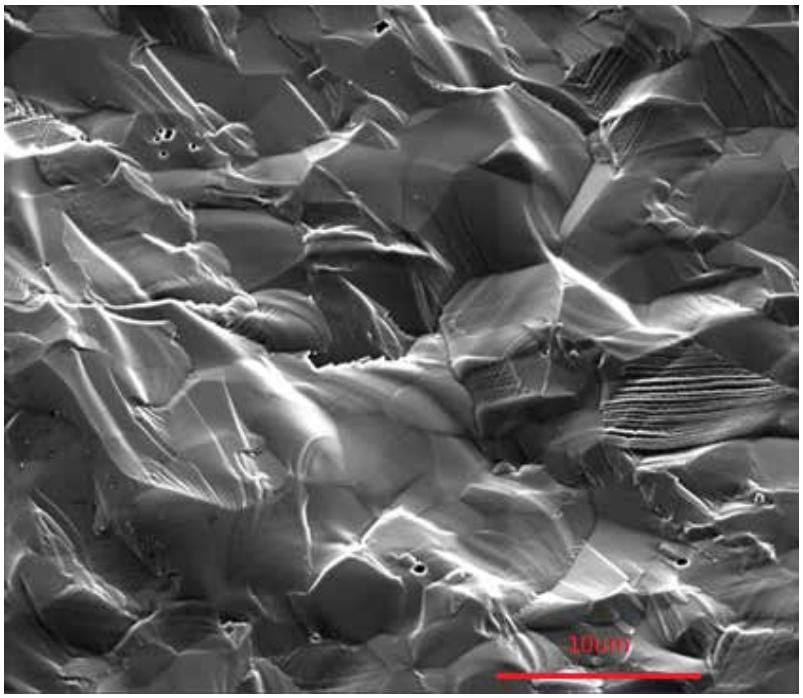

Figure 21 – High Magnification SEM Image of B4C Fracture Surface

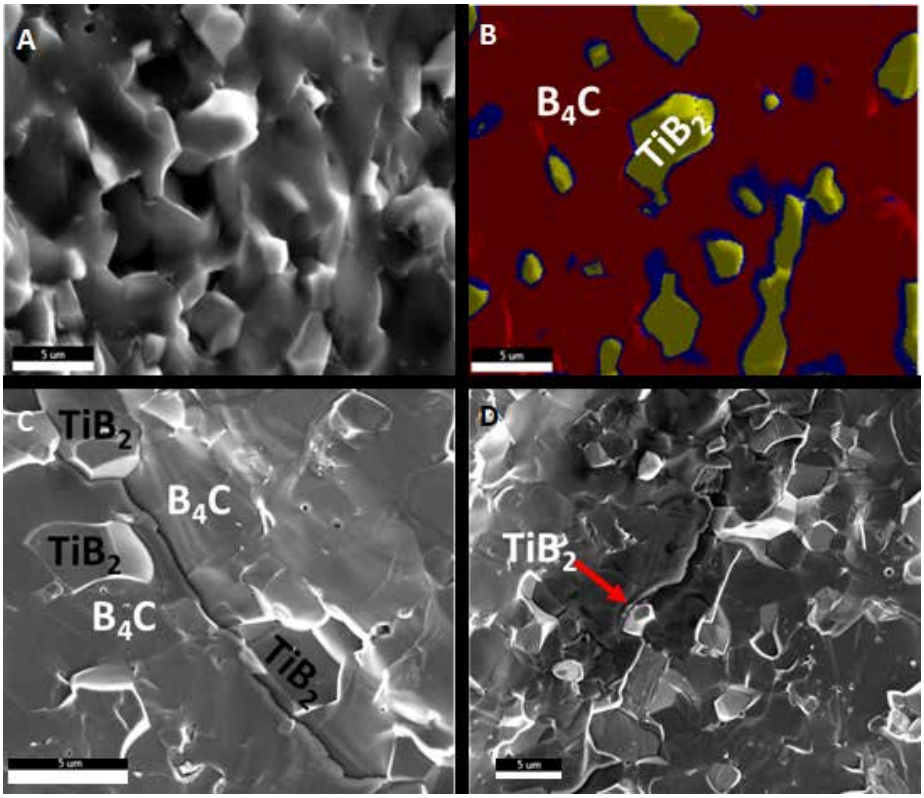

Figure 22 - (A) SEM Image and Corresponding (B) EDS Map of B4C-40%TiB2 Fracture Surface. (C,D) SEM Images of B4C-40%TiB2 Fracture Surfaces Showing Crack Deflection Around TiB2 Grains

CHAPTER 5

CONCLUSION AND FUTURE WORK

Spark plasma sintering was used in this study due to its ability to quickly and effectively sinter Boron Carbide and Titanium Diboride, two traditionally difficult to sinter ceramics. A selection of compositions was optimized and compared to commercial armor-grade ceramics to make a material with equivalent or lower density but potentially superior properties. The processing, structure, and property relationships of these materials and their composites were examined through a variety of techniques, qualitative and quantitative.

Through carefully controlled processing, this study produced monolithic Boron Carbide as well as Composites of Boron Carbide and Titanium Diboride which showed significant improvements in both mechanical and fracture properties compared to armor-grade PAD-B4C and Silicon Carbide. The use of SPS to sinter relatively pure B4C allowed for fully densified compacts without the graphite inclusions from reactive synthesis that impair its mechanical properties. The use of SPS to sinter the B4C and TiB2 composite also achieved high theoretical density that showed significant promise over its density equivalent Silicon Carbide. Additionally, the fracture toughness of the composite improved significantly over pure B4C. Collectively the improved strength and fracture resistance are a result of no residual graphitic carbon in SPS B4C-TiB2 composites, interfacial microcrack toughening mechanisms due to thermal expansion coefficient differences and residual stress states, and the crack deflection, blunting, and bridging added by the TiB2 phase.

There is significant potential for future work both in a higher standard of quantitative analysis of the reactions and for the statistics of the feed-stocks. The use of

nanometer powders and or wet milling, both mentioned briefly, also show some promise. There is potential for a strongly bimodal, or much wider, distribution which could aid in densification. There is ongoing work using nitrogen processing atmospheres to promote the formation of various nitrides to promote intergranular fracture. Lastly, dynamic high strain rate testing is of paramount importance to compare to currently used armor-grade materials. It would useful to determine how important are traditional quasi-static properties like the reported hardness, fracture toughness and flexural (bend) strength that are typically measured by ceramists when they develop and design new materials for ballistic applications. How well do these static strength and toughness properties correlate (and which one(s) are important) to dynamic, high strain rate properties. The inter-relationships between these properties will hopefully provide future insight into long standing questions on how relevant/important are traditional quasi-static strength and toughness measurements and corresponding mechanisms, such as the ones reported in this thesis.

REFERENCES

ASTM B962-17 Test Methods for Density of Compacted or Sintered Powder Metallurgy (PM) Products Using Archimedes Principle. West Conshohocken, PA, 2018, doi: 10.1520/b0962-17

ASTM C1161-18 Test Method for Flexural Strength of Advanced Ceramics at Ambient Temperature. West Conshohocken, PA, 2017, doi:10.1520/C1161-18

Baharvandi, H. R., Hadian, A. M., & Alizadeh, A. (2006, 5). Processing and Mechanical Properties of Boron Carbide–Titanium Diboride Ceramic Matrix Composites. Applied Composite Materials, 13, 191-198.

Bale, C. W., Bélisle, E., Chartrand, P., Decterov, S. A., Eriksson, G., Gheribi, A. E., et al. (2016). FactSage Thermochemical Software and Databases (Calphad ed., Vol. 54).

Basu, B., Raju, G. B., & Suri, A. K. (2006, 12). Processing and properties of monolithic TiB2based materials. International Materials Reviews, 51, 352-374.

Bullett, D. W. (1982, 1). Structure and bonding in crystalline boron and B12C3. Journal of Physics C: Solid State Physics, 15, 415-426.

Chuvashova, I., Bykova, E., Bykov, M., Svitlyk, V., Dubrovinsky, L., & Dubrovinskaia, N. (2017, 8). Structural stability and mechanism of compression of stoichiometric B13C2 up to 68GPa. Scientific Reports, 7.

Hammersley, A. (1997). FIT2D: an introduction and overview. ESRF Internal Report ESRF97HA02T.

Heydari, M. S., & Baharvandi, H. R. (2015, 7). Comparing the effects of different sintering methods for ceramics on the physical and mechanical properties of B4C–TiB2 nanocomposites. International Journal of Refractory Metals and Hard Materials, 51, 224-232.

Huang, S. G., Vanmeensel, K., Malek, O. J., Biest, O. V., & Vleugels, J. (2011, 1). Microstructure and mechanical properties of pulsed electric current sintered B4C–TiB2 composites. Materials Science and Engineering: A, 528, 1302-1309.

Hulbert, D. M., Anders, A., Dudina, D. V., Andersson, J., Jiang, D., Unuvar, C., et al. (2008, 8). The absence of plasma in “spark plasma sintering”. Journal of Applied Physics, 104, 033305.

Ji, W., Rehman, S. S., Wang, W., Wang, H., Wang, Y., Zhang, J., et al. (2015, 10). Sintering boron carbide ceramics without grain growth by plastic deformation as the dominant densification mechanism. Scientific Reports, 5.

Klam, H. J., Hahn, H., & Gleiter, H. (1987, 8). The thermal expansion of grain boundaries. Acta Metallurgica, 35, 2101-2104.

Lönnberg, B. (1988, 7). Thermal expansion studies on the group IV–VII transition metal diborides. Journal of the Less Common Metals, 141, 145-156.

McCuiston, R. C., LaSalvia, J. C., & Moser, B. (2007). Effect of Carbon Additions and B4C Particle Size on the Microstructure and Properties of B4C - TiB2 Composites. In Mechanical Properties and Performance of Engineering Ceramics and Composites III (pp. 257-268). John Wiley & Sons, Inc.

Munro, R. G. (2000, 9). Material properties of titanium diboride. Journal of Research of the National Institute of Standards and Technology, 105, 709.

Niihara, K., Morena, R., & Hasselman, D. P. (1983). Indentation Fracture Toughness of Brittle Materials for Palmqvist Cracks. In Fracture Mechanics of Ceramics (pp. 97-105). Springer US.

Pilladi, T. R., Panneerselvam, G., Anthonysamy, S., & Ganesan, V. (2012, 7). Thermal expansion of nanocrystalline boron carbide. Ceramics International, 38, 3723-3728.

Quinn, G. D. (n.d.). Fracture Toughness of Ceramics by the Vickers Indentation Crack Length Method: A Critical Review. In Mechanical Properties and Performance of Engineering Ceramics II: Ceramic Engineering and Science Proceedings, Volume 27, Issue 2 (pp. 45-62). John Wiley & Sons, Inc.

Rudy, E., Windisch, S., Ternary phase equilibria in transition-metal-boron-carbon-silicon systems. Part II. Ternary systems. Vol. XIII. Phase diagrams of the systems Ti-B-C, Zr-B-C, and Hf-B-C, Report No. AFML-TR-65-2, Air Force Materials Laboratory, Wright-Patterson Air Force Base, Ohio, 1966.

Sano, T., Shaeffer, M., Vargas-Gonzalez, L., & Pomerantz, J. (2013, 8). High Strain Rate Performance of Pressureless Sintered Boron Carbide. In Dynamic Behavior of Materials, Volume 1 (pp. 13-19). Springer International Publishing.

Setter, N. (1995, 1). Weighty tomes. Structure and Properties of Ceramics. Edited byM. V. Swain. volume 11 of Materials Science and Technology: A Comprehensive Treatment, edited by R. W. Cahn, P. Haasen, and E. J. Kramer, VCH, Weinheim 1994, 841 pp., hardcover, DM 450.00, ISBN 3-527-26824-3. Advanced Materials, 7, 175-258.

Taya, M., Hayashi, S., Kobayashi, A. S., & Yoon, H. S. (1990, 5). Toughening of a Particulate-Reinforced Ceramic-Matrix Composite by Thermal Residual Stress. Journal of the American Ceramic Society, 73, 1382-1391.

Tsagareishvili, G. V., Nakashidze, T. G., Jobava, J. S., Lomidze, G. P., Khulelidze, D. E., Tsagareishvili, D. S., et al. (1986, 3). Thermal expansion of boron and boron carbide. Journal of the Less Common Metals, 117, 159-161.

Uygun, B., Göller, G., Yücel, O., Sahin, F. (2010, 10). Production and Characterization of Boron Carbide – Titanium Diboride Ceramics by Spark Plasma Sintering Method. Advances in Science and Technology, 63, 68-73.

Vargas-Gonzalez, L., Speyer, R. F., & Campbell, J. (2010, 2). Flexural Strength, Fracture Toughness, and Hardness of Silicon Carbide and Boron Carbide Armor Ceramics. International Journal of Applied Ceramic Technology, 7, 643-651.